PARK15/FBXO7 is dispensable for PINK1/Parkin mitophagy in iNeurons and HeLa cell systems

Felix Kraus[1,2], Ellen A. Goodall[1,2], Ian R. Smith[1], Yizhi Jiang[1], Julia C. Paoli[1], Jiuchun Zhang[1], Joao A. Paulo[1], and J. Wade Harper[1,2*]

[1]Department of Cell Biology, Blavatnik Institute, Harvard Medical School, 240 Longwood Ave, Boston MA 02115, USA
[2]Aligning Science Across Parkinson's (ASAP) Collaborative Research Network, Chevy Chase, MD 20815, USA
*Correspondence: wade_harper@hms.harvard.edu (J.W.H.)

ABSTRACT

The protein kinase PINK1 and ubiquitin ligase Parkin promote removal of damaged mitochondria via a feed-forward mechanism involving ubiquitin (Ub) phosphorylation, Parkin activation, and ubiquitylation of mitochondrial outer membrane proteins to support recruitment of mitophagy receptors. The ubiquitin ligase substrate receptor FBXO7/PARK15 is mutated in an early-onset parkinsonian-pyramidal syndrome. Previous studies have proposed a role for FBXO7 in promoting Parkin-dependent mitophagy. Here, we systematically examine the involvement of FBXO7 in depolarization-dependent mitophagy in the well-established HeLa and induced-neurons cell systems. We find that FBXO7$^{-/-}$ cells have no demonstrable defect in: 1) kinetics of pUb accumulation, 2) pUb puncta on mitochondria by super-resolution imaging, 3) recruitment of Parkin and autophagy machinery to damaged mitochondria, 4) mitophagic flux, and 5) mitochondrial clearance as quantified by global proteomics. Moreover, global proteomics of neurogenesis in the absence of FBXO7 reveals no obvious alterations in mitochondria or other organelles. These results argue against a general role for FBXO7 in Parkin-dependent mitophagy and point to the need for additional studies to define how FBXO7 mutations promote parkinsonian-pyramidal syndrome.

INTRODUCTION

Organelle quality control underlies cellular health and is often defective in disease and pathological states. Arguably the best understood such quality control pathway is mitophagy, wherein damaged or supernumerary mitochondria are targeted for removal from the cell via selective autophagy (Goodall *et al*, 2022; Harper *et al*, 2018; McWilliams & Muqit, 2017; Pickrell & Youle, 2015). In this process, individual organelles are marked for sequestration within a double-membrane vesicle called an autophagosome, which then fuses with a lysosome to facilitate degradation of the organelle by resident lysosomal hydrolases (Dikic & Elazar, 2018; Stolz *et al*, 2014). Multiple forms of mitophagy have been reported, which differ in the types of regulatory mechanisms involved in marking the organelle for degradation, but these fall into two primary types – ubiquitin-dependent and ubiquitin-independent (Harper *et al.*, 2018; Pickrell & Youle, 2015). Our understanding of ubiquitin-dependent mitophagy has been advanced by the discovery of a signalling pathway composed of the PINK1 protein kinase and the Parkin (also called PRKN) ubiquitin (Ub) E3 ligase, which marks damaged mitochondria for elimination (Narendra *et al*, 2008). Parkin and PINK1 are both mutated in early-onset recessive forms of Parkinson's disease and understanding how these enzymes work has been a major focus of the field (Ng *et al*, 2021; Pickrell & Youle, 2015).

In healthy mitochondria, PINK1 is imported into the mitochondrial translocon and rapidly processed for degradation (Jin *et al*, 2010; Yamano & Youle, 2013). In response to mitochondrial damage – such as depolarization, accumulation of mitochondrial misfolded proteins, or defects in mitochondrial fusion – PINK1 is stabilized on the mitochondrial outer membrane (MOM) in association with the translocon (Lazarou *et al*, 2012), where it can phosphorylate Ser65 on Ub already conjugated to proteins on the MOM (Kane *et al*, 2014; Kazlauskaite *et al*, 2015; Koyano *et al*, 2014; Ordureau *et al*, 2014; Wauer *et al*, 2015). Accumulation of phospho S65-Ub (referred to henceforth as pUb) on the MOM promotes recruitment of Parkin – a pUb-binding protein – thereby facilitating phosphorylation of Parkin on S65 of its N-terminal Ub-like (UBL) domain and activation of its Ub ligase activity (Gladkova *et al*, 2018; Kane *et al.*, 2014; Kazlauskaite *et al.*, 2015; Ordureau *et al.*, 2014; Sauve *et al*, 2018; Wauer *et al.*, 2015). Parkin then ubiquitylates numerous MOM proteins, resulting in both the accumulation of additional pUb and further MOM protein ubiquitylation (Antico *et al*, 2021; Bingol *et al*, 2014; Ordureau *et al*, 2020; Sarraf *et al*, 2013). MOM ubiquitylation then promotes recruitment of selective autophagy cargo receptors including OPTN, CALCOCO2 (also called NDP52), and SQSTM1 (also called p62) to facilitate the assembly of an autophagosome around the ubiquitylated organelle (Evans & Holzbaur, 2020; Heo *et al*, 2015; Lazarou *et al*, 2015; Wong & Holzbaur, 2014). Thus, PINK1, Parkin, and pUb function in a positive feedback loop to promote selective ubiquitylation and elimination of the damaged organelle (Goodall *et al.*, 2022).

Previous work (Burchell *et al*, 2013) concluded that FBXO7, the product of an early-onset parkinsonian-pyramidal syndrome risk gene also designated as *PARK15* (Di Fonzo *et al*, 2009; Houlden & Singleton, 2012; Paisan-Ruiz *et al*, 2010), is a positive modulator of Parkin-dependent mitophagy (**Supplemental Figure 1A**). FBXO7 is a member of the F-box family of proteins, which assemble with SKP1, CUL1, and RBX1 to form a modular SCF Ub ligase complex wherein the F-box protein to binds substrates (Jin *et al*, 2004). FBXO7 is characterized by an N-terminal UBL domain, a central FP domain with structural similarity to a domain in the proteasome inhibitory factor PI31/PSMF1, followed by the F-box motif, and a C-terminal proline rich region (Kirk *et al*, 2008). Patient mutations in FBXO7 are found in multiple regions of the protein (Di Fonzo *et al.*, 2009; Houlden & Singleton, 2012; Paisan-Ruiz *et al.*, 2010). Initial studies on FBXO7 proposed a functional interaction with the Parkin/PINK1 pathway and concluded that FBXO7 functions as a positive regulator of mitophagy through direct interaction with Parkin and with PINK1 (Burchell *et al.*, 2013). Depletion of FBXO7 by siRNA in cell lines was reported to reduce depolarization-dependent loss in mitochondria based on immunoblotting of matrix proteins and likewise to reduce depolarization-dependent ubiquitylation of MFN1, a substrate of Parkin (Burchell *et al.*, 2013). However, studies that further substantiate a functional link between FBXO7 and

92 mitophagy are lacking, although FBXO7 depletion has recently been reported to alter
93 mitochondrial dynamics (Al Rawi *et al*, 2022).
94 Given the strong genetic association of FBOX7/PARK15 with Parkinson's Disease
95 (Houlden & Singleton, 2012) and major advances in our understanding of Parkin-dependent
96 mitophagy (Goodall *et al.*, 2022) since initial links between FBXO7 and mitophagy were
97 reported, we set out to elucidate how FBXO7 might function within the positive feedback
98 loop to promote mitophagy (**Supplemental Figure 1A**). Relevant advances include the
99 identification of pUb as a sentinel response to PINK1/Parkin activation (Kane *et al.*, 2014;
100 Kazlauskaite *et al.*, 2015; Koyano *et al.*, 2014; Ordureau *et al.*, 2014; Wauer *et al.*, 2015),
101 the development of highly quantitative mitophagic flux assays using a mitochondrially
102 localized Keima fluorescent reporter protein (Katayama *et al*, 2011; Lazarou *et al.*, 2015),
103 and the development of genetically tractable iNeuron systems for functional analysis of the
104 Parkin pathway in neuronal cell types (Ordureau *et al.*, 2020; Ordureau *et al*, 2018).
105 Unexpectedly, we find no evidence of a role for FBXO7 in the kinetics of depolarization-
106 dependent pUb accumulation, or mitophagic flux in either iNeurons or the conventional HeLa
107 cell used extensively to examine Parkin and PINK1-dependent mitophagy (Narendra *et al.*,
108 2008). Moreover, global proteomics of FBXO7$^{-/-}$ HeLa cells undergoing mitophagy revealed
109 no defect in mitochondrial elimination by autophagy. Taken together with previous studies
110 that failed to verify Parkin-FBXO7 interactions during mitophagy (Sarraf *et al.*, 2013), these
111 data indicate that FBXO7 does not play a general role as a positive modulator of Parkin and
112 PINK1-dependent mitophagy in HeLa and iNeuron systems. This work suggests that
113 elucidation of FBXO7 biochemical functions is needed to understand how it might contribute
114 to suppression of early-onset parkinsonian-pyramidal syndrome.
115
116 **RESULTS**
117 ***A tool kit for functional analysis of cells lacking FBXO7***
118 To test if FBXO7 is a pivotal amplifier of the PINK1/Parkin pathway, we employed
119 CRISPR-Cas9-based gene editing to generated knockouts for FBXO7 in HeLa HFT/TO-
120 PRKN cells (Ordureau *et al*, 2015) and confirmed insertion of a frameshift mutation by
121 sequencing and immunoblotting (**Supplemental Figure 1 B-D**). HeLa HFT/TO-PRKN cells
122 contain a DOX-inducible PRKN cassette allowing regulated expression of Parkin to facilitate
123 an analysis of mitophagic flux in response to mitochondrial damage (Ordureau *et al.*, 2015).
124 Three independent FBXO7$^{-/-}$ clones were identified (clones 27, 41 and 45) (**Supplemental**
125 **Figure 1C,D**). In parallel, we generated two independent human ES cell clones lacking
126 FBXO7 via CRISPR-Cas9 (clones 52 and 89) (**Supplemental Figure 1B,E,F**). Here, an ES
127 cell line harbouring a DOX inducible NGN2 gene was used, allowing for conversion of these
128 cells to cortical-like iNeurons over a two week or greater time course (Ordureau *et al.*, 2020;

129 Zhang *et al*, 2013). We have previously demonstrated that iNeurons derived from these cells
130 exhibit Parkin and PINK1-dependent mitophagic flux in response to mitochondrial damage
131 (Ordureau *et al.*, 2020). Both clones displayed normal karyotypes and the absence of
132 FBXO7 was verified using MiSeq sequencing (**Supplemental Figure 1F,G**).
133

134 ***Robust depolarization-dependent Ub phosphorylation by PINK1 in cells lacking***
135 ***FBXO7***

136 The earliest known event in Parkin-dependent mitophagy is accumulation of PINK1
137 on the mitochondrial outer membrane followed by rapid S65 phosphorylation of pre-existing
138 Ub linked with mitochondrial proteins (**Supplemental Figure 1A**), as has been worked out in
139 detail using the well-validated HeLa cell system with ectopically expressed Parkin (Kane *et*
140 *al.*, 2014; Lazarou *et al.*, 2012; Narendra *et al*, 2010; Yamano & Youle, 2013). In the
141 presence of Parkin, Ub phosphorylation is enhanced as a result of increased Ub conjugation
142 to mitochondrial proteins, thereby providing additional substrate molecules for
143 phosphorylation by PINK1 (Kane *et al.*, 2014; Koyano *et al.*, 2014; Ordureau *et al.*, 2014). To
144 examine pUb accumulation in the context of HeLa cells lacking FBXO7, we induced Parkin
145 expression (16 h) and then depolarized mitochondria for 1 or 6 h with antimycin
146 A/Oligomycin A (AO), which inhibit Complex III and Complex IV activity in the electron
147 transport chain, respectively. As expected, control HeLa cells display time-dependent
148 accumulation of pUb as measured by immunoblotting, but the absence of FBXO7 had no
149 impact on the extent of pUb accumulation, as assessed in all three FBXO7$^{-/-}$ cell lines in
150 biological triplicate analyses (**Figure 1A,B**).

151 Similarly, we assessed depolarization-dependent pUb accumulation in the iNeuron
152 system. control or FBXO7$^{-/-}$ ES cells were converted to day 12 iNeurons and depolarized
153 with AO in duplicate (**Figure 1C**). pUb was detected by immunoblotting at 6 and 24 h and
154 was indistinguishable between WT and two independent FBXO7$^{-/-}$ clones (**Figure 1D**).
155 Taken together, these data do not support a universal role for FBXO7 in promoting the
156 earliest step in mitophagy signalling – PINK1-dependent Ub phosphorylation – in the HeLa
157 cell system or iNeurons.
158

159 ***Super-resolution imaging of pUb formation independent of FBXO7***

160 While depolarization-dependent Ub phosphorylation was not impaired, we
161 considered the possibility that the organization of pUb on damaged mitochondria might be
162 altered in cells lacking FBXO7. To our knowledge, super-resolution microscopy has not been
163 used to examine the kinetics and spatial properties of pUb accumulation in response to
164 depolarization. We therefore optimized conditions to monitor pUb via volumetric 3D-SIM
165 super-resolution microscopy in both HeLa and iNeuron systems (see **EXPERIMENTAL**

166 **MATERIALS AND METHODS**). After AO treatment of HeLa cells for 1, 3 or 6 h, the
167 mitochondria matrix protein HSP60 and pUb were examined by super-resolution imaging. In
168 control cells at 1 h, fragmented mitochondria were often proximal to pUb foci with an
169 average volume of 5.71 μm^3, which were not observed in cells lacking PINK1 (**Figure 2A-C,**
170 **Supplemental Figure 2A,B**). The volume of pUb increased ~8-fold over 6 h (47.88 μm^3),
171 consistent with the known feed-forward response (**Figure 2B, Supplemental Figure 2A**). At
172 6 h of AO treatment, we observed a near complete coating of mitochondrial fragments with
173 pUb, as quantified by the significant increase in pUb object volume (**Figure 2B,C,**
174 **Supplemental Figure 2A**). Consistent with analysis of pUb by immunoblotting, two FBXO7$^{-/-}$
175 clones did not show any significant differences in pUb recruitment, volume or overall
176 morphological differences compared to control cells, indicating that FBXO7 is not required
177 for the feed-forward amplification of PINK1/Parkin mitophagy after AO-treatment (**Figure 2A-**
178 **C**). Analogous super-resolution experiments in day 12 iNeurons with 0.5, 1, and 3 h of AO
179 revealed similar results, with no obvious effect of FBXO7 deletion on pUb recruitment,
180 volume or overall morphology when compared to WT iNeurons (**Figure 2D-F,**
181 **Supplemental Figure 3A**). As expected (Ordureau *et al.*, 2020; Ordureau *et al.*, 2018),
182 iNeurons lacking PINK1 did not accumulate pUb (**Figure 2D,E**). These results were also
183 confirmed in iNeurons treated with AO for 1 or 6 h using conventional immunofluorescence
184 and image analysis of HSP60 and pUb co-localization (**Figure 2G,H**). To ensure that kinetic
185 effects were not obscured by overt depolarization, we reduced the concentrations of AO
186 used by 10-fold, but again no defect in pUb recruitment to mitochondria was observed
187 (**Supplemental Figure 3B,C**). These data indicate that the absence of FBXO7 does not
188 alter the ability of PINK1-dependent pUb foci to accumulate on damaged mitochondria in
189 either HeLa or iNeuron systems.
190

191 ***Parkin and autophagy regulator recruitment in FBXO7$^{-/-}$ cells***

192 Parkin recruitment depends upon the accumulation of pUb on damaged mitochondria
193 (**Supplemental Figure 1A**) (Okatsu *et al*, 2015). Given that the existing model for FBXO7 in
194 Parkin-dependent mitophagy posited that Parkin and FBXO7 physically interact and that
195 FBXO7 promotes Parkin function (Burchell *et al.*, 2013), we directly tested whether FBXO7
196 is required for Parkin recruitment to mitochondria using the HeLa cell system. Control or
197 FBXO7$^{-/-}$ cells were stably transduced with a lentivirus expressing GFP-Parkin and subjected
198 to imaging with or without depolarization with AO (**Supplemental Figure 4A**). We used
199 CellProfiler (Stirling *et al*, 2021) to analyse the characteristics of GFP-Parkin and
200 mitochondria and their relationship to each other. By segmenting out cytosolic and
201 mitochondrially-localized Parkin, we could quantify alterations in Parkin abundance within
202 the mitochondrial mask as a measure of Parkin-translocation (**Supplemental Figure 4B**).

203 Our expectation was that a requirement for FBXO7 in Parkin recruitment would result in
204 reduced Parkin intensity within the mitochondrial mask in response to depolarization. First,
205 we tested whether mitochondrial morphology (mitochondrial integrated density [==mtIntDen]
206 as proxy, stained with HSP60) is changing after AO-treatment on a single-cell level. Under
207 fed conditions, control and three FBXO7$^{-/-}$ clones displayed comparable mtIntDen.
208 Depolarization by AO led to the expected mitochondrial fragmentation and clustering, thus
209 causing an increase in local HSP60 signal and a right-shift in mtIntDen (**Supplemental**
210 **Figure 4C, top panel**). This shift was also observed to a similar extend in FBXO7$^{-/-}$ cells.
211 Thus, both control and FBXO7$^{-/-}$ cells robustly respond to AO-induced mitophagy. Next, we
212 tested if Parkin intensities are increasing on mitochondria on an "organelle object" level. As
213 expected, mtIntDen did shift to the right after AO-treatment, in line with previous
214 experiments. Parkin signal was comparable between the genotypes under fed conditions,
215 and increased in intensity after AO-treatment, consistent with Parkin accumulation inside the
216 mitochondrial area (**Supplemental Figure 4C, lower panel**). This Parkin shift was observed
217 in both control and FBXO7$^{-/-}$ cell lines, arguing that FBXO7 is not universally required for
218 Parkin recruitment to damaged mitochondria.

219 Mitochondrial ubiquitylation by Parkin promotes recruitment of downstream
220 autophagy machinery, including the FIP200-ULK1 complex and Ub-bind autophagy
221 adaptors, ultimately leading to the formation of an autophagosome (Heo *et al.*, 2015;
222 Lazarou *et al.*, 2015; Ravenhill *et al*, 2019; Vargas *et al*, 2019). Lipidation of LC3 is
223 associated with autophagosome formation and is thought to contribute to recruitment of
224 autophagy receptors. As expected, depolarization of Parkin-expressing HeLa cells resulted
225 in recruitment of both p62 and FIP200 to mitochondria in a manner that dependent on
226 PINK1, as revealed by immunostaining and confocal imaging (**Supplemental Figure 4D**).
227 However, FBXO7$^{-/-}$ cells were as proficient as control cells in recruitment of p62 or FIP200
228 after 3 h or 16 h or AO-induced mitophagy (**Supplemental Figure 4D-G**). Previous studies
229 using siRNAs targeting FBXO7 also reported that LC3 lipidation in response to mitochondrial
230 depolarization is defective compared with non-depleted cells (Burchell *et al.*, 2013).
231 However, all three FBXO7$^{-/-}$ HeLa cell clones underwent depolarization-dependent LC3
232 lipidation to similar extents, consistent with a functional Parkin pathway (**Supplemental**
233 **Figure 4H,I**). Taken together, these data indicate that FBXO7 is not universally required to
234 promote either Parkin-dependent recruitment to damaged mitochondria or subsequent steps
235 that depend upon Ub chain assembly on mitochondria such as recruitment of autophagy
236 machinery and initiation of LC3 lipidation.

237 Additionally, we have not able to reproduce a previously reported association
238 between overexpressed FBXO7 and PINK1 (Huang *et al*, 2020) in either HEK293T or
239 HCT116 cells. Briefly, as part of our BioPlex project (Huttlin *et al*, 2021), we ectopically

240 expressed PINK1-HA and performed interaction proteomics. While we identified the known
241 protein kinase chaperone HSP90 subunits in association with PINK1, we did not detect
242 FBXO7 (**Supplemental Figure 4J, left panel; Supplemental Table S1**). Likewise, FBXO7
243 associated reciprocally with members of the CUL1-SKP1-RBX1, the COP9/Signalosome,
244 and both core particle and regulatory subunits of the proteasome in HEK293T and/or
245 HCT116 cells, as expected (Bader *et al*, 2011; Liu *et al*, 2019; Vingill *et al*, 2016), but neither
246 PINK or Parkin were detected (**Supplemental Figure 4J,K; Supplemental Table S2**)
247 (Huttlin *et al.*, 2021) (see **METHODS**). These results are consistent with our previous Parkin
248 interaction proteomics experiments that failed to demonstrate an interaction with FBXO7
249 during mitophagy induction (Sarraf *et al.*, 2013).
250
251 ***Mitophagic flux in FBXO7$^{-/-}$ cells***
252 A significant advance has been the development of mitophagy reporters, which
253 cumulatively measure flux of mitochondrial turnover through to the final stages of mitophagy:
254 the fusion of mitochondria-laden autophagosomes with lysosomes (Lazarou *et al.*, 2015).
255 mKeima is a fluorescent protein that undergoes a pH-dependent Stokes shift, and delivery of
256 a Keima-tagged cargo from the cytoplasm to the acidic interior of the lysosome can be
257 monitored by measuring the ratio of emission at 620 nm with maximal excitation at 440 nm
258 or 586 nm under neutral or acidic conditions, respectively, by flow cytometry or microscopy
259 (**Figure 3A**). To monitor differences in mitophagic flux upon deletion of FBXO7, we
260 employed mtKeima, an mKeima protein targeted to the mitochondrial with a COX8-matrix
261 targeting sequence (Ordureau *et al.*, 2020).
262 In Parkin-expressing HeLa cells, the ratio of acidic-Keima (measured with excitation
263 at 561 nm and emission 620 nm) to neutral Keima (ex. 405 nm, em. 603 nm) increases as
264 cells are treated with AO (**Figure 3B, Supplemental Figure 4L**). This mitophagic flux is
265 PINK1-dependent as deletion of PINK1 abolishes this shift (**Figure 3B, Supplemental**
266 **Figure 4L**). As expected, there is little flux without depolarization with AO, and inhibition of
267 the lysosomal V-ATPase with BafilomycinA1 (BafA) restores the mtKeima acidic:neutral ratio
268 to levels similar to that seen fed cells (**Supplemental Figure 4L**). In three FBXO7$^{-/-}$ clones,
269 AO-dependent mitophagic flux is similar to control cells with increasing flux observed with
270 increasing length of AO treatment (**Figures 3B; Supplemental Figure 4L**). We validated the
271 mtKeima flux results using the mitochondrial DNA clearance assay (Heo *et al.*, 2015;
272 Lazarou *et al.*, 2015). Staining for mtDNA foci per cell after 24 h AO treatment in control and
273 FBXO7$^{-/-}$ HeLa cells showed a significant decrease in mtDNA number in all samples (**Figure**
274 **3G**). The remaining mtDNA levels were indistinguishable between control and FBXO7$^{-/-}$ cells
275 (**Figure 3G**).

276 We also measured mtKeima foci and flux in control and FBXO7$^{-/-}$ iNeurons at day 12
277 of differentiation (**Figure 3C-E**). As with HeLa cells, red-shifted mtKeima foci increased ~2-
278 fold after 6 h AO treatment in control and FBXO7$^{-/-}$ cells (**Figure 3C,D**). Using flow
279 cytometry, mitophagic flux (normalized to BafA) after 6 and 24 h AO treatment was
280 comparable between control and FBXO7$^{-/-}$ iNeurons, and was absent in PINK1$^{-/-}$ cells
281 (**Figure 3E**). Additionally, we investigated mtDNA turnover in d12 control and two
282 independent FBXO7$^{-/-}$ iNeuron clones. Within 6 or 24 h of depolarization of iNeurons, we
283 observed a reduction in the number of mitochondrial DNA/cell, and the effect was
284 independent of the presence or absence of FBXO7 (**Figure 3F,G**). Taken together, these
285 data indicate that FBXO7 is not universally required for depolarization-dependent mitophagic
286 flux in either the HeLa or iNeuron systems.
287
288 ***Proteomic analysis of HeLa cells lacking FBXO7 during mitophagy***
289 As an alternative to mtKeima for measuring mitophagic flux, we examined the total
290 proteome of depolarized HeLa cells with the expectation that in control HeLa cells,
291 mitochondrial turnover would result in bulk loss of the mitochondrial proteome in depolarized
292 cells. Thus, control or FBXO7$^{-/-}$ HeLa cells expressing Parkin were depolarized for 16 h in
293 triplicate and total cell extracts subjected to 18-plex Tandem Mass Tagging (TMT)-based
294 proteomics (**Figure 4A, Supplemental Table S3,S4**) (Li *et al*, 2021). Replicates were highly
295 correlated, with correlation coefficients greater that 0.95 and Principal Component Analysis
296 (PCA) revealed tight clustering of replicates, with the major feature separating the samples
297 being AO-treatment (**Supplemental Figure 5A,B**). Through hierarchical clustering
298 (**Supplemental Figure 5C**), we identified major alterations in the abundance of mitochondria
299 in response to depolarization (**Figure 4B, Supplemental Figure 5D-I**). Indeed, the majority
300 of proteins annotated as mitochondrial were found to have reduced levels in control cells in
301 response to depolarization, as indicated in the overlap of mitochondrial proteins on the
302 volcano plots for the ~8000 proteins quantified (leftward skew of red dots in **Figure 4B**, left
303 panel). Importantly, the patterns of protein abundance were indistinguishable from control for
304 two independent FBXO7$^{-/-}$ cell lines, with leftward skew of mitochondrial proteins in the
305 volcano plot (**Figure 4B,C**). Proteins with altered abundance were enriched for mitochondrial
306 matrix, inner membrane, outer membrane and oxidative phosphorylation categories,
307 consistent with autophagy of entire organelles (**Figure 4C**). The behaviour of other
308 organelles and large protein complexes were similar for both control and FBXO7$^{-/-}$ cells
309 (**Figure 4C**). Moreover, both FBXO7 clones displayed similar behaviour to each other and to
310 the control, as indicated by correlation analysis (Pearson's R=0.82, 0.86 and 0.74,
311 respectively) (**Figure 4D,E**). These results are consistent with the absence of a discernible
312 alteration in depolarization-dependent mitophagic flux in cells lacking FBXO7. A previous

313 report proposed that depletion of FBXO7 resulted in accumulation of PINK1 proteins levels
314 under basal conditions (Huang *et al.*, 2020), but in our experiments, PINK1 levels in the two
315 FBXO7$^{-/-}$ clones were unaffected based on TMT intensities (**Figure 4F**).
316
317 ***Proteomic analysis of human ES cells lacking FBXO7 during neurogenesis***
318 As an initial unbiased approach to examining FBXO7 function in iNeurons, we
319 performed 18-plex TMT proteomics on control and two clones of FBXO7$^{-/-}$ cells at day 0, 4
320 and d12 of differentiation (**Figure 5A, Supplemental Table S5-S8**). We have previously
321 demonstrated dramatic remodelling of mitochondria around day 4 of differentiation to
322 support a switch from glycolysis to oxidative phosphorylation, which is accompanied by
323 BNIP3L-dependent mitophagy of a fraction of mitochondria (Ordureau *et al*, 2021). From the
324 ~6000 proteins quantified across all replicates and conditions, we found strong
325 correspondence of control and FBXO7$^{-/-}$ cells, with PC1 being drive by differentiation
326 (**Supplemental Figure 6A,B**). FBXO7 itself was expressed at comparable levels across the
327 time course but was not detected in FBXO7$^{-/-}$ iNeurons, as expected (**Supplemental Figure**
328 **6C**). Remarkably, the abundance of the proteome was largely immune to the loss of FBXO7
329 at both day 4 and day 12 of differentiation (**Figure 5B-D, Supplemental Figure 6D**).
330 Moreover, the abundance of mitochondrial proteins (including inner and out membrane and
331 OXPHOS components) were unchanged relative to control cells at day 4 or 12 of
332 differentiation (**Figure 5B, Supplemental Figure 6D**).
333 Recent reports have directly linked L250P mutations in the dimerization domain of
334 FBXO7 to MiD49/MiD51, a core adapter protein involved in mitochondrial fission (Al Rawi *et*
335 *al.*, 2022). Indeed, DNM1L-mediated mitochondrial fission has been previously indicated in
336 the efficient scission of damaged parts of mitochondria and protection of the remaining
337 healthy mitochondrial network (Burman *et al*, 2017). Cells expressing FBXO7^{L250P} were
338 found to have reduced levels of proteasome subunits as well (Al Rawi *et al.*, 2022). Our
339 proteomic data from iNeurons indicates no alterations in the abundance of proteasome
340 subunits or mitochondrial fission and fusion machinery (DNM1L, MFF, and MiD51) in
341 iNeurons lacking FBXO7 (**Figure 5C,E**). To test if loss of FBXO7 causes in morphological
342 changes in the mitochondrial network, we stained day 12 iNeurons with for the matrix marker
343 HSP60 prior to image analysis (**Figure 5F,G**). However, we observed no significant
344 alterations in the number of mitochondria/cell or the mean mitochondrial length in control or
345 FBXO7$^{-/-}$ iNeurons. The mean mitochondrial circularity was slightly reduced in FBXO7$^{-/-}$
346 iNeurons treated with AO for 3h (**Figure 5F**). Analogous analyses of mitochondria and
347 fission/fusion proteins also did not reveal significant alterations in response to loss of FBXO7
348 in two independent clones of HeLa cells (**Figure 5H,I**). However, there was a ~10%
349 decrease in the abundance of proteasome subunits in HeLa cells lacking FBXO7 in the

350 absence of depolarization, but an increase after mitophagy induction (**Supplemental Figure**
351 **5E, Figure 4C**). If this response is a compensatory mechanism of the knockout cell line to
352 cope with cytotoxic insults is an intriguing idea. Last, we examined whether FBXO7$^{-/-}$ is
353 required for the maintenance of the mitochondrial organelle pool during differentiation.
354 Previous work has shown significant metabolic rewiring during the differentiation from hESC
355 to iNeurons, including a switch from glycolysis to oxidative phosphorylation as the cells main
356 energy source (Ordureau *et al.*, 2021). Since this switch is accompanied by increased
357 mitophagy, we set out to see if the absence of FBXO7 would lead to accumulation of
358 mitochondria and/or impair differentiation. FBXO7$^{-/-}$ cells did not display obvious differences
359 in the abundance of mitochondrial proteins, when normalized to day 0 (**Figure 5B,**
360 **Supplemental Figure 6D**). Likewise, other abundance of other organelles was unchanged
361 (**Figure 5C**). Finally, neither differentiation markers or autophagy proteins displayed obvious
362 changes in control versus the two FBXO7$^{-/-}$ clones as measured by TMT-proteomics and
363 displayed using a T^2-statstic (Ordureau *et al.*, 2021) (**Supplemental Figure 7A-F**).
364

365 **DISCUSSION**

366 Despite strong genetic evidence linking mutations in FBXO7 with parkinsonian-
367 pyramidal syndrome (Di Fonzo *et al.*, 2009; Houlden & Singleton, 2012; Paisan-Ruiz *et al.*,
368 2010), our understanding of the cellular roles of FBXO7 are limited. An early study reported
369 biochemical links between FBXO7 and Parkin/PINK1-dependent mitophagy in fibroblasts
370 and SH-SY5Y cells, including interaction of overexpressed FBXO7 with both PINK1 and
371 Parkin (Burchell *et al.*, 2013). Using siRNA to deplete FBXO7, it was also concluded that
372 FBXO7 promotes Parkin's ability to ubiquitylate the outer mitochondrial membrane substrate
373 MFN1 and also promotes clearance of mitochondria by autophagy. These biochemical and
374 physiological results led to the conclusion that FBXO7 functions as a biochemical amplifier
375 of Parkin/PINK1-deepndent mitophagy (Burchell *et al.*, 2013). However, follow-up studies
376 have been limited, and the field has experienced dramatic advances in the understanding of
377 the biochemical roles of Parkin and PINK1 in promoting mitochondrial clearance by
378 autophagy, thereby providing the tools to examine potential roles of FBXO7 in the pathway.

379 With these tools, we set out to define where in the pathway FBXO7 might operate to
380 promote mitophagy. However, in both the HeLa cells with overexpressed Parkin and
381 iNeurons with a fully endogenous Parkin/PINK1 pathway, we failed to validate a role for
382 FBXO7 in any of several steps in the pathway, including pUb accumulation, Parkin
383 recruitment to the mitochondrial outer membrane, recruitment of autophagy machinery,
384 mitophagic flux as measured by mtKeima, and mitochondrial proteome degradation. The
385 finding that deletion of FBXO7 has no obvious effect on the pathway with either endogenous
386 or overexpressed Parkin in iNeurons and HeLa cells indicates that FBXO7 does not play a

387 general or universally required role in the pathway. A previous study largely based on
388 overexpression concluded that FBXO7 may bind and regulate PINK1 levels, with <2-fold
389 increases in PINK1 by immunoblotting in FBXO7-depleted cells (Huang *et al.*, 2020).
390 However, our quantitative proteomics experiments (**Figure 4**) indicated that deletion of
391 FBXO7 has no effect on PINK1 abundance, consistent with the finding that pUb
392 accumulation in response to depolarization is unaffected in FBXO7$^{-/-}$ cells. Moreover, our
393 previous interaction proteomics experiments failed to identify either PINK1 in association
394 with overexpressed FBXO7 (Huttlin *et al.*, 2021) or FBXO7 in association with
395 overexpressed Parkin (Sarraf *et al.*, 2013). Thus, our functional and biochemical results do
396 not support a biochemical linkage between FBXO7 and the PINK1-Parkin pathway.
397 In order to broadly examine FBXO7$^{-/-}$ iNeurons for pathways that are affected, we
398 performed global proteomic analysis during neurogenesis *in vitro*. However, we did not
399 observe any alterations in pathways linked with mitochondria, or other quality control
400 pathways, although a reduction in the abundance of alcohol dehydrogenase enzymes
401 among a small number of other proteins, was observed. Whether these signatures are
402 related to FBXO7 function remains to be examined. While a recent study linked the L250P
403 mutation in the dimerization domain of FBXO7 with alterations in proteins associated with
404 mitochondrial fusion and fission (Al Rawi *et al.*, 2022), we did not observe alterations in
405 either the abundance of these proteins (MiD51, MFF, FIS1) nor did we observe changes in
406 mitochondrial morphology in either HeLa cells or iNeurons lacking FBXO7.
407 An apparent ortholog of FBXO7 was identified in *Drosophila* – referred to as
408 *nutcracker*, *ntc* – and shown to associate with components of the core particle of the
409 proteasome, as well as with DmPI31 (Bader *et al.*, 2011). Association of human FBXO7 with
410 proteasome components and PI31(also called PSMF1) have also been observed in both
411 focused studies and in our previous interaction proteomic studies (Al Rawi *et al.*, 2022;
412 Huttlin *et al.*, 2021; Vingill *et al.*, 2016). In this context, PI31/DmPI31 and FBXO7/*ntc* have
413 been proposed to functionally link proteasome trafficking via dynein motors in neuronal
414 processes (Liu *et al.*, 2019). Our interaction proteomics analysis has also confirmed
415 association of FBXO7 with PSMF1, CRL, COP9/Signalosome, and proteasome core
416 subunits (**Supplemental Figure 4J,K**). Further studies are required to elucidate the
417 relationship between FBXO7 and parkinsonian-pyramidal syndrome, to understand any
418 functional relationships between FBXO7 and other Parkinson's disease risk alleles, and to
419 examine whether FBXO7's physical association with the proteasome is linked with disease.
420

421 **ACKNOWLEDGMENTS**

422 This work was supported by Aligning Science Across Parkinson's (ASAP) (J.W.H.), the NIH
423 (R01 NS083524 to J.W.H. and K01DK098285 to J.A.P.), and the Harvard Medical School

Cell Biology Initiative for Molecular Trafficking and Neurodegeneration. Michael J Fox Foundation administers the grant ASAP-000282 on behalf of ASAP and itself. For the purpose of open access, the author has applied a CC-BY public copyright license to the Author Accepted Manuscript (AAM) version arising from this submission. We thank Laura Pontano Vaites for help with the BioPlex 3.0 interactome analysis. We thank Jennifer Waters, Talley Lambert, Federico Gasparoli and Rylie Walsh in the Nikon Imaging Center and the Cell Biology Microscopy Facility (CBMF) at Harvard Medical School for microscopy support and technical support.

KEYWORDS

FBXO7, mitophagy, proteomics, iNeurons

DATA & CODE AVAILABILITY

Proteomic data and analysis files part of this study are deposited at ProteomeXchange Consortium by the PRIDE partner (Deutsch *et al*, 2020; Perez-Riverol *et al*, 2022). The PRIDE project identification number is PXD037797 and can be accessed for reviewers under username reviewer_pxd037797@ebi.ac.uk; password 65wg8SiI. Macros and pipelines used in this work can be found on GitHub (https://github.com/harperlaboratory/FBXO7.git) or Zenodo (https://doi.org/10.5281/zenodo.7258918). Raw files associated with this work are deposited on Zenodo (https://doi.org/10.5281/zenodo.7268030).

AUTHOR CONTRIBUTIONS

Study design: J.W.H., F.K., E.A.G.; Data collection: F.K., E.A.G., J.A.P., J.Z., Y.Z.; Data analysis and interpretation: F.K., E.G., I.R.S., J.A.P., J.Z., Y.Z. L.P.V.; Manuscript preparation: J.W.H., F.K. with input from all authors.

DECLARATION OF INTERESTS

J.W.H. is a consultant and founder of Caraway Therapeutics and a founding scientific advisory board member of Interline Therapeutics. No other authors declare a conflict of interest.

FIGURES

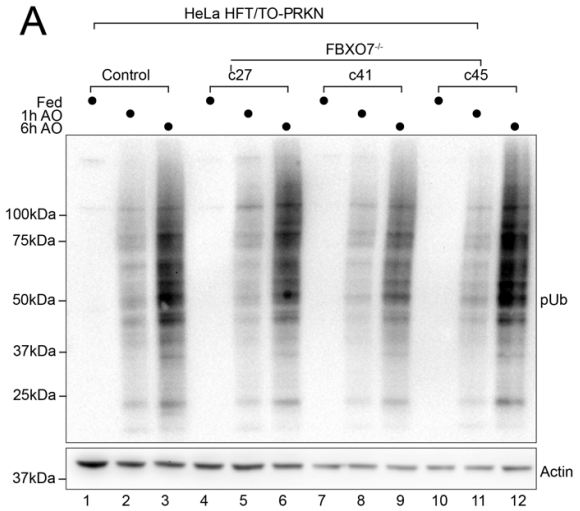
A
HeLa HFT/TO-PRKN
FBXO7-/-
Control
c27
c41
c45
Fed
1h AO
6h AO
100kDa
75kDa
50kDa
37kDa
25kDa
pUb
37kDa
Actin
1 2 3 4 5 6 7 8 9 10 11 12

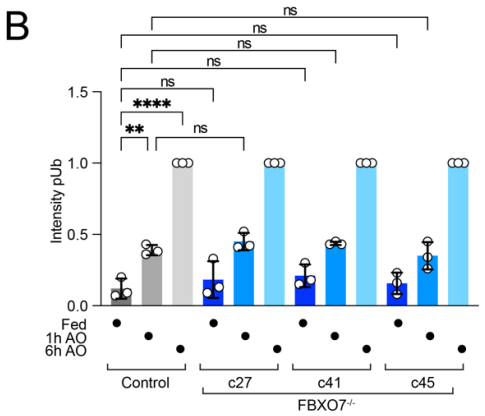
B
ns
ns
ns
ns
ns
****
**
ns
1.5
1.0
0.5
0.0
Intensity pUb
Fed
1h AO
6h AO
Control
c27
c41
c45
FBXO7-/-

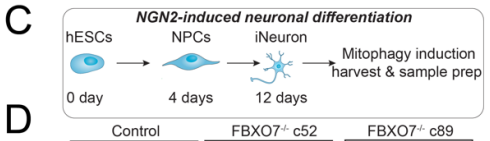
C
NGN2-induced neuronal differentiation
hESCs
NPCs
iNeuron
Mitophagy induction
harvest & sample prep
0 day
4 days
12 days

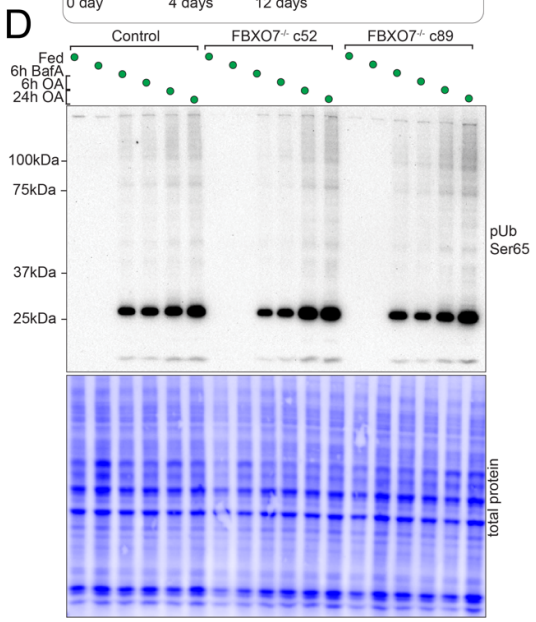
D
Control
FBXO7-/- c52
FBXO7-/- c89
Fed
6h BafA
6h OA
24h OA
100kDa
75kDa
37kDa
25kDa
pUb
Ser65
total protein

460 **Figure 1: Robust depolarization-dependent Ub phosphorylation by PINK1 cells**
461 **lacking FBXO7**. (**A**) Immunoblot for pUb on HeLa control and FBXO7$^{-/-}$ cells after treatment
462 with AO for indicated times. (**B**) Quantification of pUb signal relative to loading. Immunoblots
463 run in triplicates. Error bars depict S.D.. (**C**) Scheme depicting production of iNeurons for
464 biochemical analysis. (**D**) Immunoblot for pUb on extracts from day 12 iNeuron control and
465 FBXO7$^{-/-}$ cells after treatment with BafA or AO for indicated times.
466
467

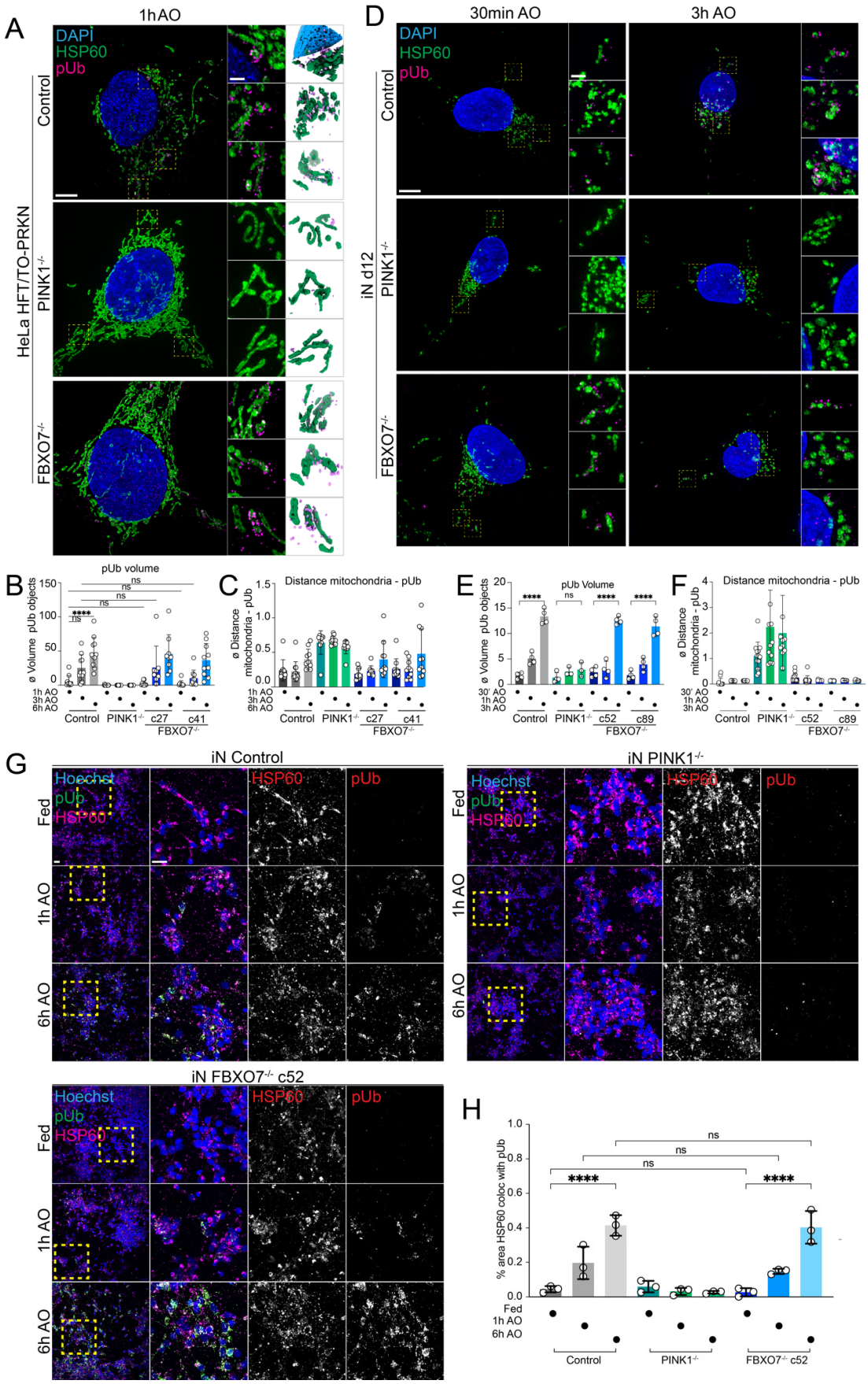
A
1h AO
DAPI
HSP60
pUb
Control
PINK1-/-
FBXO7-/-
HeLa HFT/TO-PRKN
D
30min AO
3h AO
iN d12
B
pUb volume
ø Volume pUb objects
1h AO
3h AO
6h AO
Control
PINK1-/-
c27
c41
FBXO7-/-
C
Distance mitochondria - pUb
ø Distance mitochondria - pUb
E
pUb Volume
30' AO
c52
c89
F
G
iN Control
iN PINK1-/-
Hoechst
Fed
iN FBXO7-/- c52
H
% area HSP60 coloc with pUb
ns
****

469 **Figure 2. Super-resolution imaging of pUb formation independent of FBXO7.** (**A**) 3D-
470 SIM images of HeLa control, PINK1$^{-/-}$ and FBXO7$^{-/-}$ cell lines after AO-induced mitophagy.
471 Cells were stained for nuclear DNA (DAPI), mitochondria (HSP60) and pUb. Zoom-ins of
472 regions of interested are enlarged in the middle panel. 3D-surface renderings of insets are
473 shown on the right. Scale bar = 5 µm or 1 µm. (**B,C**) Evaluation of 3D-SIM images from
474 HeLa datasets. The changes in pUb volume and minimal distances between mitochondria
475 and pUb after mitophagy-induction are plotted. Error bars depict S.D. from 8-14 measured
476 cells per condition. (**D**) 3D-SIM images of iN day 12 control, PINK1$^{-/-}$ and FBXO7$^{-/-}$ cell lines
477 after AO-induced mitophagy. Cells were stained for nuclear DNA (DAPI), mitochondria
478 (HSP60) and pUb. Zoom-ins of regions of interested are enlarged in the middle panel. 3D-
479 surface renderings of insets are shown on the right. Scale bar = 5 µm or 1 µm. (**E,F**)
480 Evaluation of 3D-SIM images from iNeuron datasets. The changes in pUb volume and
481 minimal distances between mitochondria and pUb after mitophagy-induction are plotted.
482 Error bars depict S.D. from 7-14 measured cells per condition. (**G**) Confocal images of
483 iNeuron d12 Control, PINK1$^{-/-}$ and FBXO7$^{-/-}$ cell lines after AO-induced mitophagy. Cells
484 were stained for nuclear DNA (Hoechst33342), mitochondria (HSP60) and pUb. Scale bar =
485 10µm and 5µm. (**H**) Evaluation of pUb volume after mitophagy induction. Error bars depict
486 S.D. from 3 replicates.
487
488

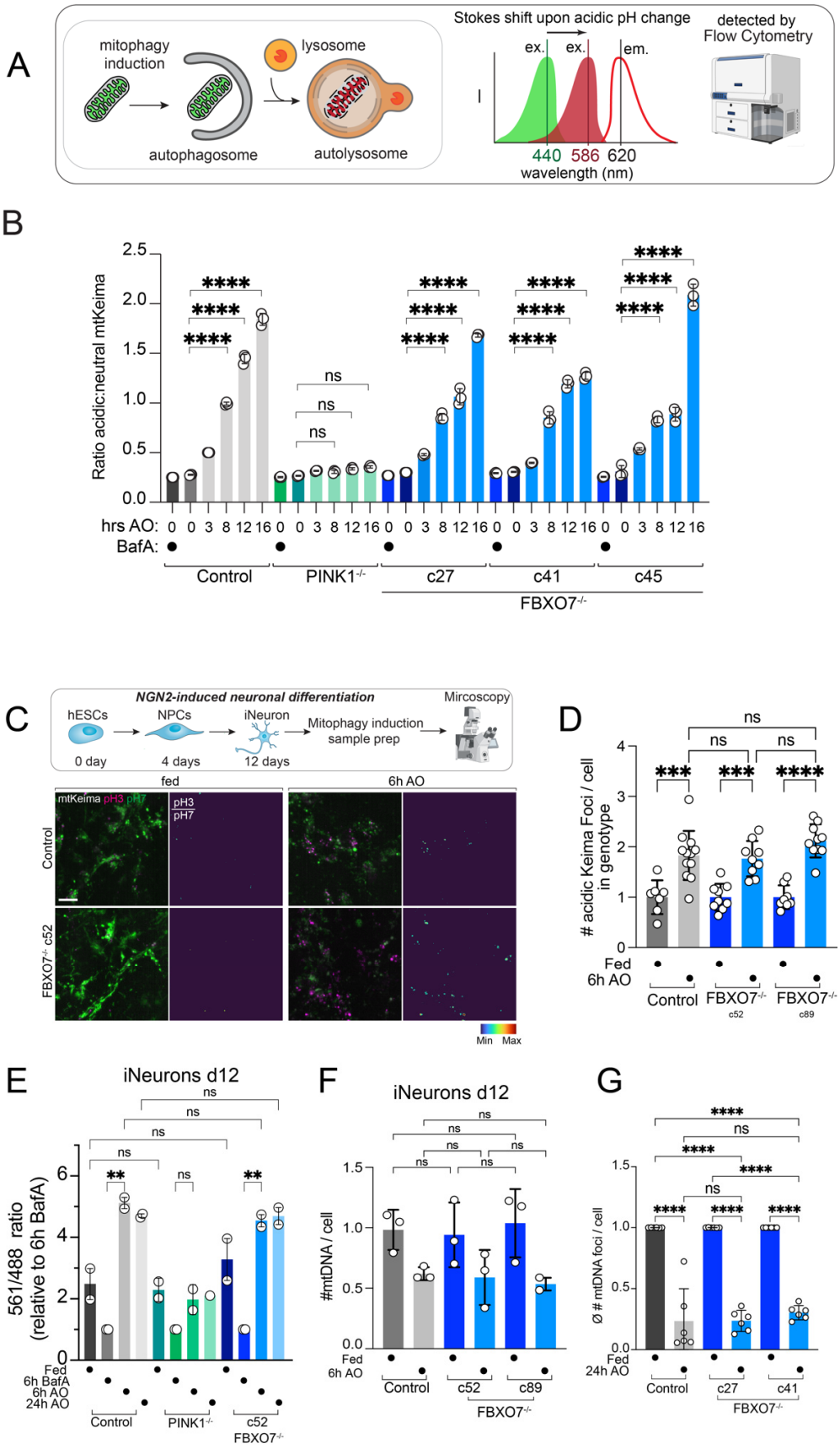
A
mitophagy induction
lysosome
autophagosome
autolysosome
Stokes shift upon acidic pH change
ex.
ex.
em.
I
440 586 620
wavelength (nm)
detected by Flow Cytometry
B
Ratio acidic:neutral mtKeima
hrs AO: 0 0 3 8 12 16 0 0 3 8 12 16 0 0 3 8 12 16 0 0 3 8 12 16 0 0 3 8 12 16
BafA:
Control
PINK1-/-
c27
c41
c45
FBXO7-/-
C
NGN2-induced neuronal differentiation
hESCs
NPCs
iNeuron
Mitophagy induction sample prep
Mircoscopy
0 day
4 days
12 days
fed
6h AO
mtKeima pH3 pH7
pH3
pH7
Control
FBXO7-/- c52
Min Max
D
acidic Keima Foci / cell in genotype
Fed
6h AO
Control
FBXO7-/- c52
FBXO7-/- c89
E
iNeurons d12
561/488 ratio (relative to 6h BafA)
Fed
6h BafA
6h AO
24h AO
Control
PINK1-/-
c52
FBXO7-/-
F
iNeurons d12
#mtDNA / cell
Fed
6h AO
Control
c52
c89
FBXO7-/-
G
Ø # mtDNA foci / cell
Fed
24h AO
Control
c27
c41
FBXO7-/-

490 **Figure 3. Mitophagic flux in iNeurons and HeLa cells lacking FBXO7.** (**A**) Scheme
491 depicting mitophagic flux assay using mtKeima. See text for details. (**B**) Mean Acidic:Neutral
492 mtKeima per-cell ratios measured by flow cytometry for HeLa cells expressing Parkin
493 ndicating the number of hours treated with AO (Antimycin A (0.5 μM) and Oligomycin (0.5
494 μM)) or three hours with 25 nM BafilomycinA (BafA). Error bars depict S.D. from triplicate
495 measurements. (**C**) Indicated hESCs expressing mtKeima were differentiated to iNeurons
496 (day 12) and were subjected to image analysis. Scale bar, 5 μm. (**D**) The number of red-
497 shifted Keima foci per cell is plotted, where each dot represents the average foci-number per
498 image stack, originating from 7-12 image stacks of iNeuron differentiations. Error bars
499 represent S.D.. (**E**) mtKeima mitophagy flux readout of indicated iNeuron genotypes. Cells
500 were treated with AO for either 1 or 6h and mitophagic flux measured by flow cytometry
501 (>10,000 cells). Pooled data from 2 biological replicates is shown, normalized to 6h BafA
502 treated cells. Error bars depict S.D.. (**F**) Bar graph showing the number of mtDNA
503 puncta/cell with or without treatment with AO (6 h) in control or FBXO7$^{-/-}$ day 12 iNeurons.
504 Error bars depict S.D. from triplicate differentiations. (**G**) Bar graph showing the number of
505 mtDNA puncta/cell with or without treatment with AO (6 h) in HeLa control or FBXO7$^{-/-}$ cells.
506 Error bars depict S.D. from triplicate replicates.
507
508

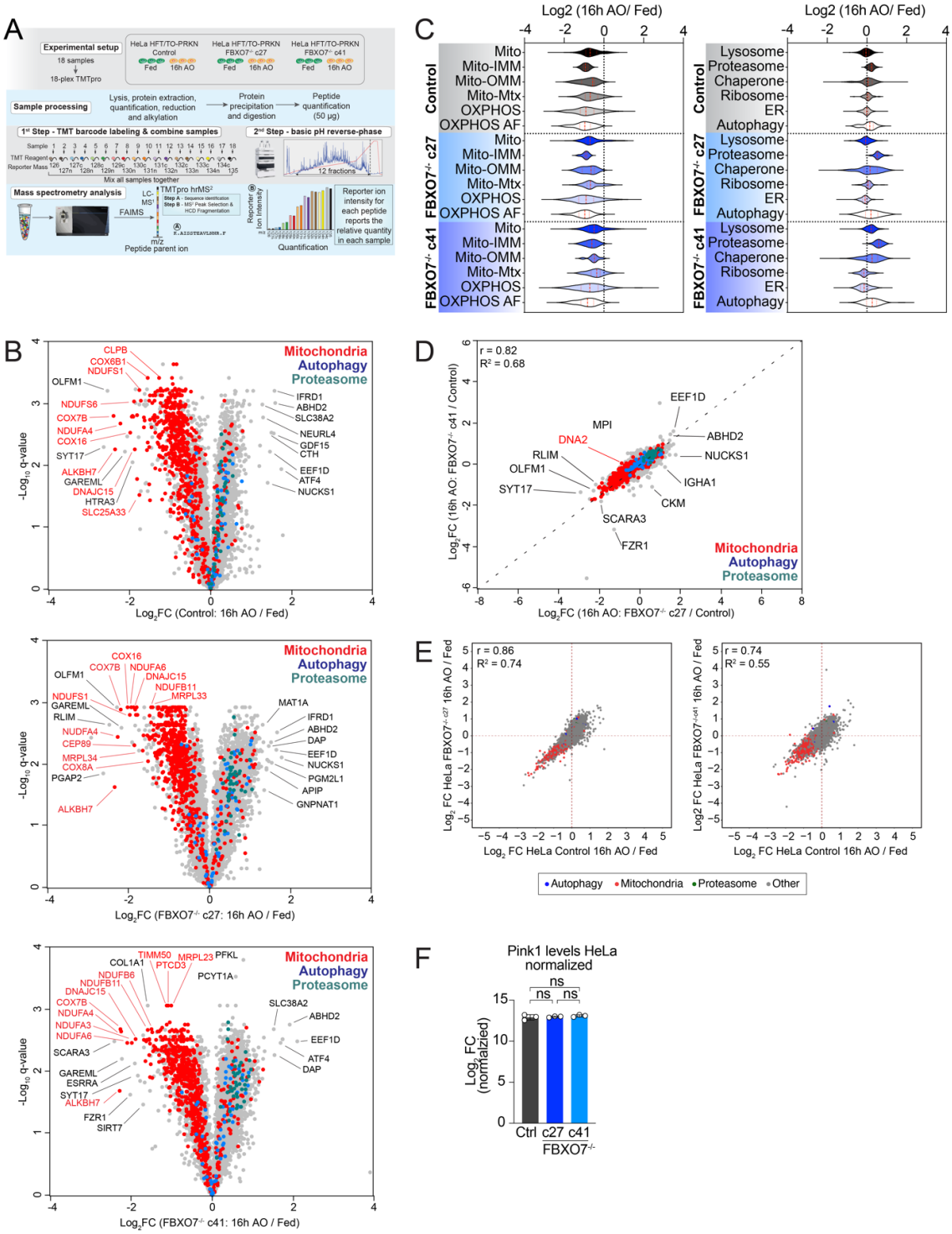

Figure 4. Proteomic analysis of HeLa cells lacking FBXO7 during mitophagy. (**A**) Workflow for analysis of total protein abundance in HeLa cells expressing Parkin with and without depolarization with AO (16 h). Cell extracts were digested with trypsin prior to 18-plex TMT labelling and analysis by mass spectrometry. (**B**) Volcano plots [Log_2 FC (16 h AO / Fed) versus -Log_{10}(q-value)] for control or one of two FBXO7$^{-/-}$ cell lines with or without treated with AO (16 h). Red dots, mitochondrial proteins; blue dots, autophagy proteins; grey dots, remainder of the proteome. (**C**) Violin plots [Log_2 (16 h AO/Fed)] of control or FBXO7$^{-/-}$ cells depicting alterations in the abundance of mitochondrial protein (left panel) or specific

518 organelles or protein complexes (right panel). (**D**) Correlation plot of c27 and c41 FBXO7$^{-/-}$
519 clones. Log_2FC (16 h AO for each clone relative to control cells) is plotted. (**E**) Correlation
520 plots [Log_2 FC (16 h AO / Fed)] of the proteome of FBXO7$^{-/-}$c27 or c41 clones against
521 control. Red dots, mitochondrial proteins; blue dots, autophagy proteins; grey dots,
522 remainder of the proteome. (**F**) PINK1 levels in control cells and in two FBXO7$^{-/-}$ clones were
523 measured by TMT-proteomics in fed cells (n=3).
524
525

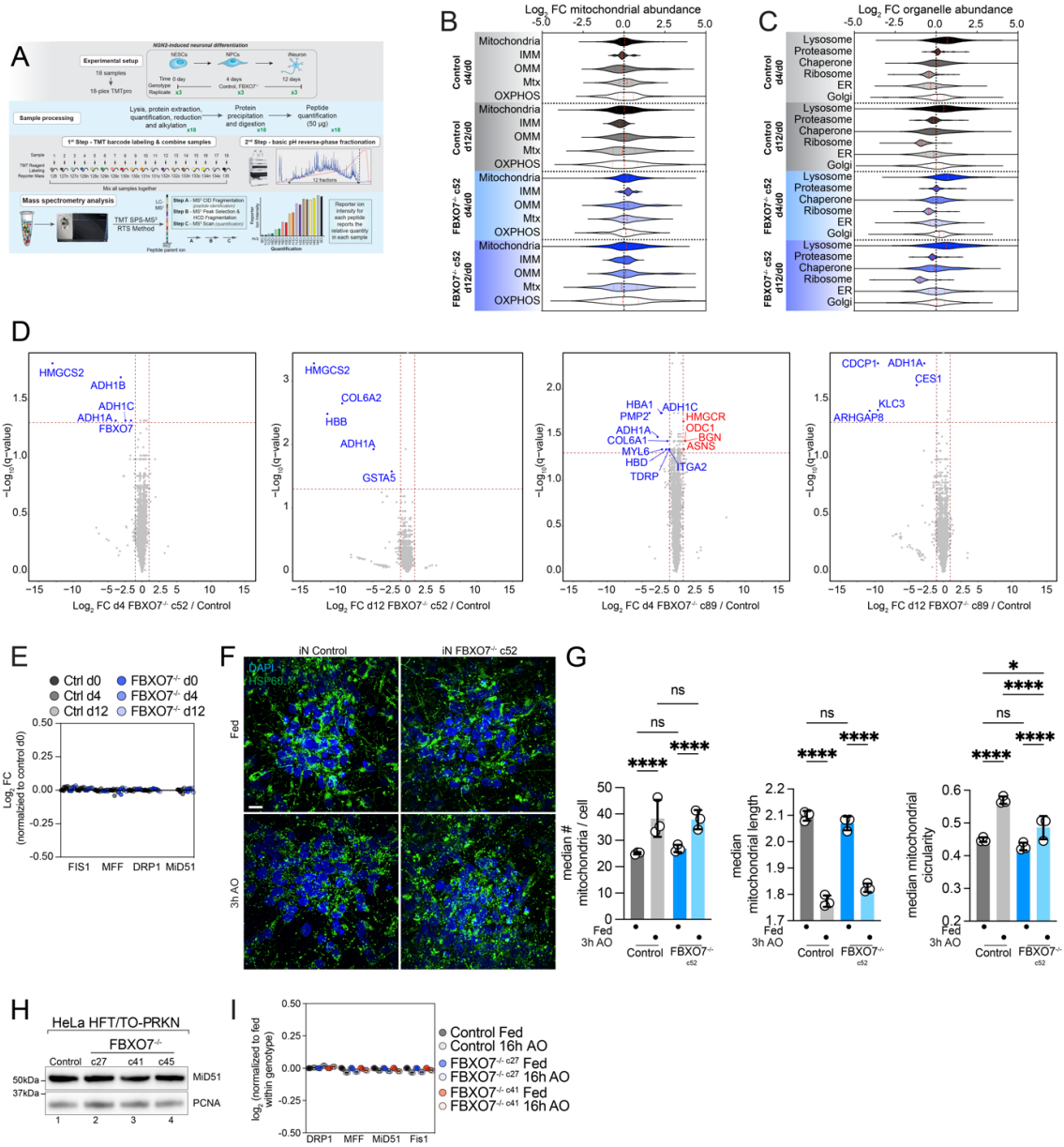

Figure 5. Proteomic analysis of human ES cells lacking FBXO7 during neurogenesis. (A) Workflow for analysis of total protein abundance in ES cells undergoing NGN2-driven neurogenesis with or without FBXO7. Cell extracts were digested with trypsin prior to 18-plex TMT labelling and analysis by mass spectrometry. (**B**) Log_2 FC for the indicated mitochondrial protein-groups in control or FBXO7$^{-/-}$ cells at day 0, 4 or 12 during neurogenesis is shown in violin plots. (**C**) Log_2 FC for the indicated cellular organelle proteins in control or FBXO7$^{-/-}$ cells at day 0, 4 or 12 during neurogenesis is shown in violin plots. (**D**) Volcano plots [Log_2 FC (FBXO7$^{-/-}$/Control) versus -Log_{10}(q-value)] for FBXO7$^{-/-}$ (c52 and c89) and control cells at day 4 (left panel) or day 12 (right panel) of differentiation. Proteins showing decreased or increased abundance are shown as blue or red dots. (**E**) Relative abundance of DNM1L (Drp1), MFF, and FIS1 in control or FBXO7$^{-/-}$ cells at day 0, 4 or 12 during neurogenesis. (**F,G**) Mitochondrial morphology in iNeurons (iN) was assessed using confocal imaging after staining cells with HSP60 to detect mitochondria and DAPI to identify nuclei, in either fed cells or cells treated with AO (3 h) (left panel). The number of median # of mitochondria/cell, median mitochondrial length, and median mitochondrial circularity is shown. Error bars depict S.D. from biological triplicate experiments (9-12 image

543 stacks each), as shown in panel I left, center, and right, respectively. (**H**) Western Blot
544 analysis on HeLa control and FBXO7$^{-/-}$ whole cell lysate, probed for the mitochondrial fission
545 adapter MiD51. (**I**) Relative abundance of DNM1L, MFF, MiD51 and FIS1 in WT (Control) or
546 FBXO7$^{-/-}$ HeLa cells either in the fed state or after 16 h AO as determined from the
547 proteomics data in **Figure 5A,B**.
548
549

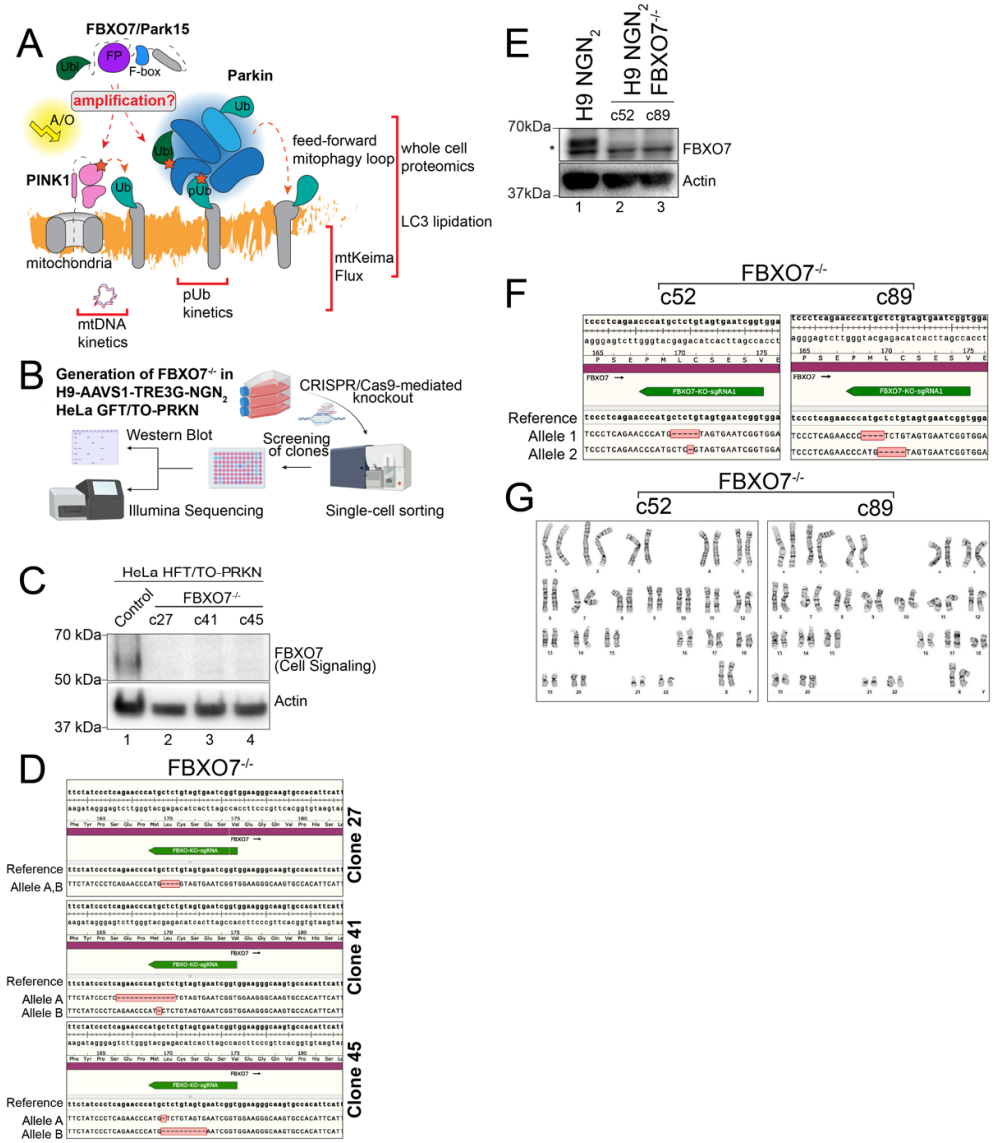

Supplemental Figure 1: Tool kit for analysis of HeLa cells and iNeurons lacking FBXO7. (**A**) Working model summarizing the suggested modes of action of FBXO7 in PINK1/Parkin mitophagy. (**B**) Targeting of gRNA sequence within FBXO7 gene along with the sequences of alleles A and B. MiSeq analysis of the three clones used for this study are shown. (**B**) Schematic for generation of FBXO7$^{-/-}$ in hESC cell lines. (**C**) Western Blot analysis on HeLa control and FBXO7$^{-/-}$ whole cell lysate. (**D**) Targeting of gRNA sequence within FBXO7 gene along with the sequences of alleles A and B. MiSeq analysis of the three HeLa clones (c27, c41, c45) used for this study are shown. (**E**) Western Blot analysis on hESC control and FBXO7$^{-/-}$ whole cell lysate. Asterisk indicates non-specific band. (**F**) Targeting of gRNA sequence within FBXO7 gene along with the sequences of alleles A and B. MiSeq analysis of the two clones (c52, c89) used for this study are shown. (**G**) Karyotype analysis of FBXO7$^{-/-}$ c52 and c89 hESCs.

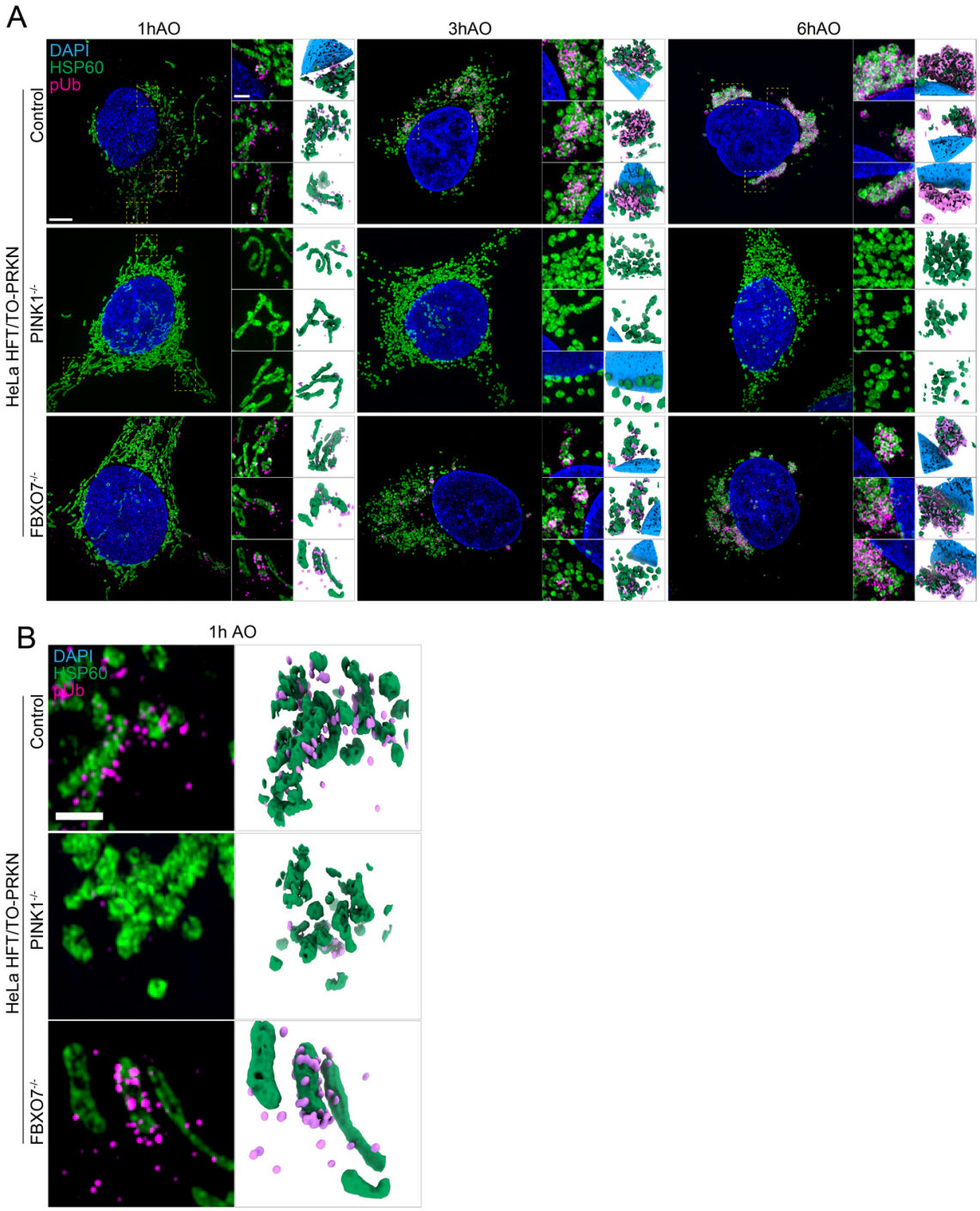

Supplemental Figure 2. Super-resolution pUb detection in HeLa cells in response to mitochondrial depolarization. 3D-SIM images of HeLa control, PINK1$^{-/-}$ and FBXO7$^{-/-}$ cell lines after 1h, 3h or 6h, AO-induced mitophagy (related to **Figure 2A,B**). Cells were stained for nuclear DNA (DAPI), mitochondria (HSP60) and pUb. (**B**) Zoom-ins of regions of interested after 1h AO-induced mitophagy are depicted and 3D-surface renderings of insets are shown on the right. Scale bar = 5 µm or 1 µm.

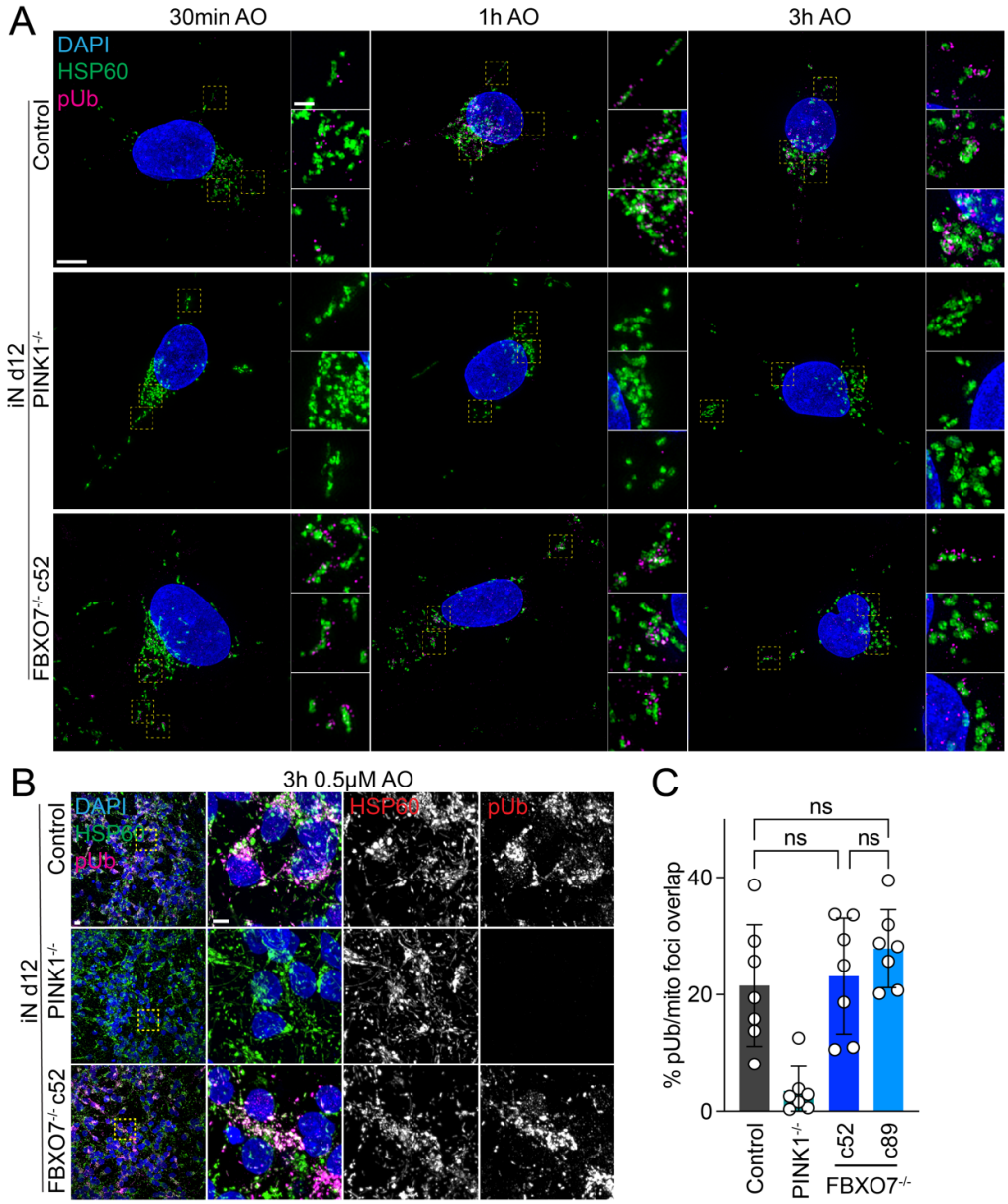

Supplemental Figure 3. Super-resolution pUb detection in iNeurons in response to mitochondrial depolarization. (**A**) 3D-SIM images of iNeurons day 12 control, PINK1$^{-/-}$ and FBXO7$^{-/-}$ cell lines after AO-induced mitophagy. Cells were stained for nuclear DNA (DAPI), mitochondria (HSP60) and pUb. Related to **Figure 2D**. Scale bar = 5 μm or 1μm. (**B**) Confocal images of iNeurons day 12 control, PINK1$^{-/-}$ and FBXO7$^{-/-}$ cell lines after AO-induced mitophagy with lower AO concentrations. Cells were stained for nuclear DNA (DAPI), mitochondria (HSP60) and pUb. (**C**) Evaluation of images depicted in **B.** Error bars depict S.D. from 12 image stacks measured per condition. Scale bar = 10 μm and 5 μm.

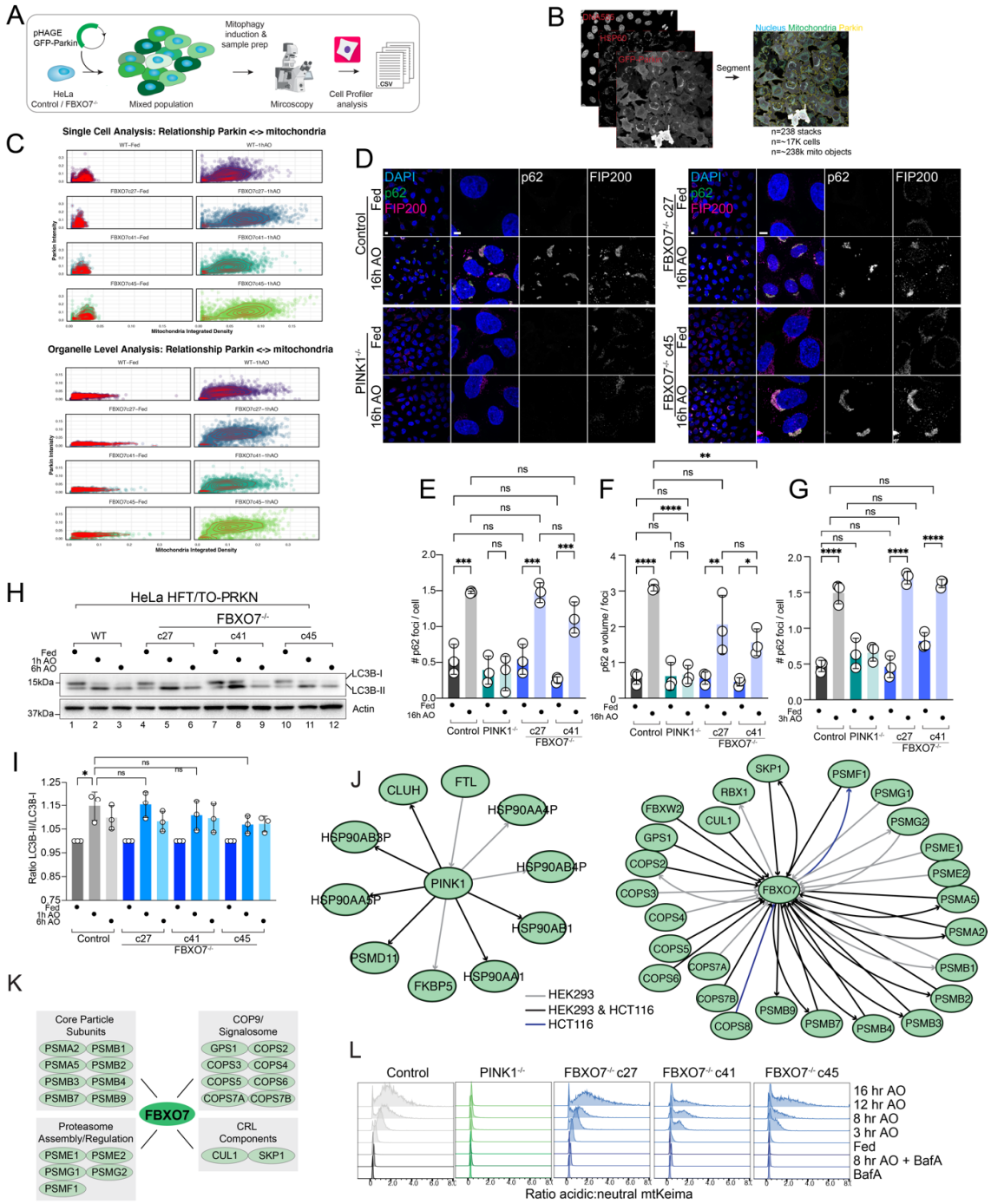

Supplemental Figure 4. Parkin and autophagy regulator recruitment in FBXO7$^{-/-}$ cells. (**A**) Overview of methods for analysis of Parkin recruitment to damaged mitochondria. (**B**) Cells were imaged for GFP-Parkin, nuclei, and mitochondria and segmented to facilitate analysis of Parkin recruitment to mitochondria in single cells / mitochondrial organelles. (**C**) Std mitochondrial signal vs Parkin intensity and Std Parkin vs mitochondria with or without 1h AO-induced mitophagy are shown. Data from three replicates, including a total of 238 image stacks, containing 16888 cells and 237848 mitochondrial objects. (**D**) Recruitment of p62 to mitochondria (not stained) in control or FBXO7$^{-/-}$ HeLa cells with or without treatment with AO (16 h) was examined by confocal imaging. Scale bar = 10 and 5 µm. (**E,F**) Quantification of cells in panel D. Assays were performed in biological triplicate with 4 image

stacks taken per repeat. n = 6712 cells. Error bars depict S.D.. (**G**) Quantification of #p62 foci normalized per cell in control, PINK1$^{-/-}$ and FBXO7$^{-/-}$ cells with or without 3h AO treatment. Assays were performed in biological triplicate with 4 image stacks taken per repeat . n = 12646 cells. Error bars depict S.D.. (**H**) Control or FBXO7$^{-/-}$ HeLa cells expressing Parkin were either left untreated or incubated with AO for 1 or 6 h and extracts subjected to immunoblotting with α-LC3B and α-Actin as a loading control. (**I**) The ratio of LC3B lipidation (LC3B-II/LC3B-I) was quantified in 3 biological triplicate experiments. (**J**) Interaction network analysis of PINK1 (left) and FBXO7 (right) based on interaction proteomics data from our BioPlex Interactome (Huttlin *et al.*, 2021) (see METHODS for details). (**K**) Summary of major interactions observed for FBXO7 in the context of the relevant protein complexes. (**L**) Ridgeline plots of mtKeima-shift analysis in HeLa control, PINK1$^{-/-}$ and FBXO7$^{-/-}$ cell lines treated with AO at the indicated times. All lines are normalized to the BafA sample.

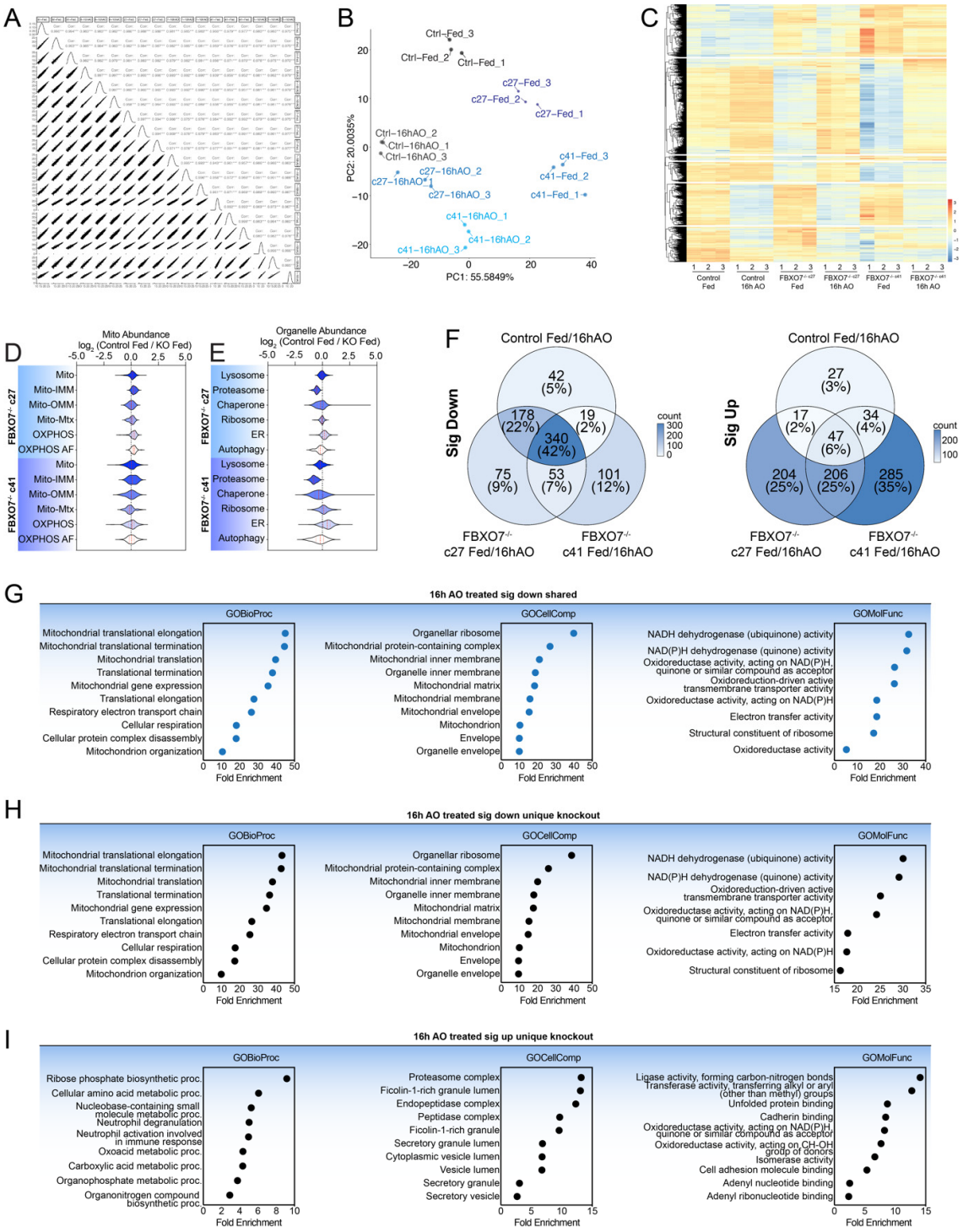

Supplemental Figure 5. Proteomic analysis of HeLa cells lacking FBXO7 during mitophagy. (**A,B**) Correlation plots (panel A) and PCA analysis (panel B) for ~8000 proteins quantified by TMT proteomics in individual replicates for the experiment outlined in **Figure 4A**. (**C**) Hierarchical clustering of 8000 proteins quantified in the experiment outlined in **Figure 4A**. (**D,E**) Violin plots [Log_2 (control / FBXO7$^{-/-}$)] for FBXO7$^{-/-}$ c27 and c41 cells depicting alterations in the abundance of mitochondrial proteins (left panel) or specific organelles or protein complexes (right panel). (**F**) Venn diagrams depicting the overlap in the number of proteins whose levels are reduced (left panel) or increased (right panel) for the

625 data shown in **Figure 4B** are shown. Proteins whose abundance is significantly reduced
626 upon AO treatment are enriched in proteins limited with mitochondrial function (right panel),
627 as expected for cells undergoing mitophagy. (**G**) GO-term enrichment analysis of genes
628 significantly down in both Control and FBXO7$^{-/-}$ after 16h AO mitophagy. (**H,I**) GO-term
629 enrichment analysis of unique genes significantly down (panel H) or up (panel I) in FBXO7$^{-/-}$
630 after 16h AO mitophagy.
631
632

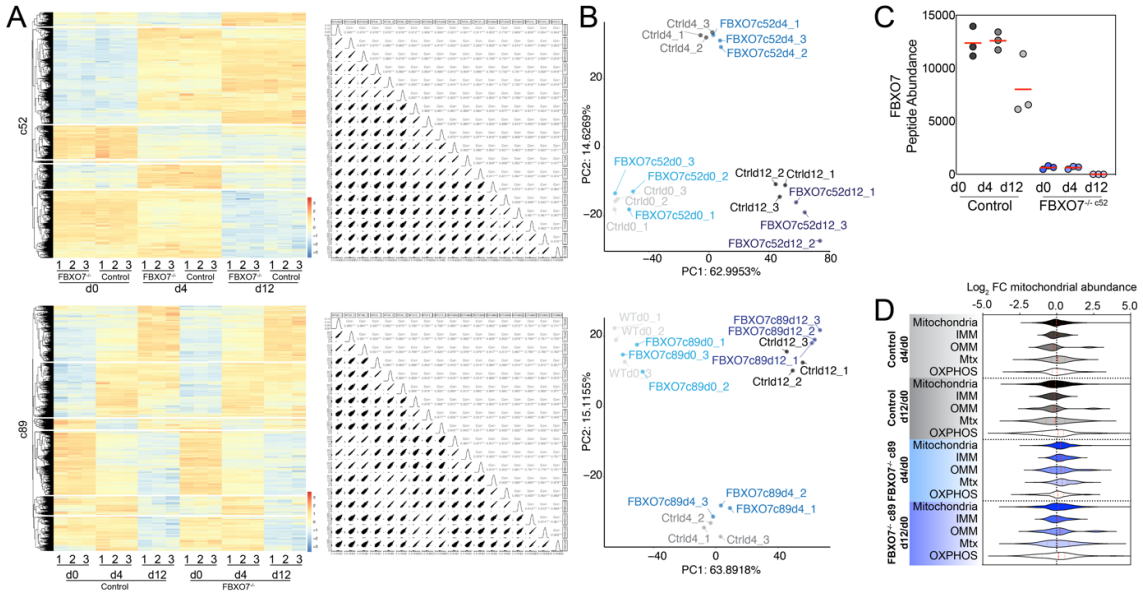

Supplemental Figure 6. Proteomic analysis of human ES cells lacking FBXO7 during neurogenesis. (**A**) Hierarchical clustering and correlation plots of control and FBXO7$^{-/-}$ c52 (top) or c89 (bottom) at indicated days of differentiation in the experiment outlined in **Figure 5A.** (**B**) PCA analysis of whole cell proteomic samples from control and FBXO7$^{-/-}$ cells. Triplicates for each timepoint and genotype were used. (**C**) FBXO7 peptide abundance in control and FBXO7$^{-/-}$ cells at indicated days of differentiation. (**D**) Violin plots [Log_2 (control / FBXO7$^{-/-}$)] for FBXO7$^{-/-}$ c89 cells depicting alterations in the abundance of mitochondrial proteins.

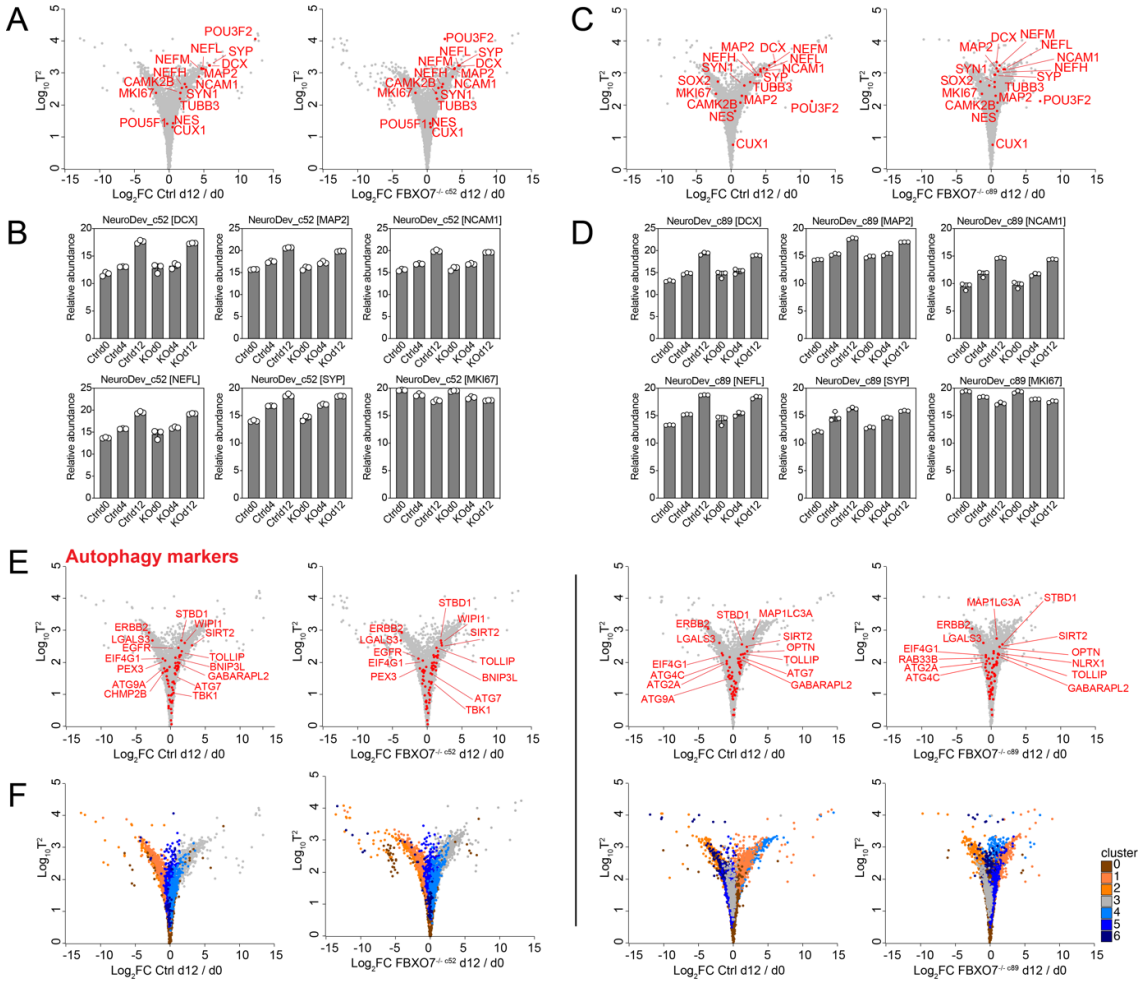

Supplemental Figure 7. Comparison of human ES cell neurogenesis with or without FBXO7. (**A**) Hotelling plots (Log_{10} T^2 statistic versus Log_2 FC day 12/day 0) of control (left panel) or FBXO7$^{-/-}$ c52 hES cells undergoing differentiation. Selected neurogenesis factors are indicated. (**B**) The relative abundance of selected proteins is shown in the lower histograms at day 0, 4 and 12 of differentiation. (**C,D**) Hotelling plots similar to **A,B** for control and FBXO7$^{-/-}$ c89. (**E**) Patterns of changes in the abundance of autophagy proteins in control (left panel) and FBXO7$^{-/-}$ (right panel) day 12 iNeurons relative to day 0 cells displayed on a Hotelling plot. (**F**) Cluster analysis of control and FBXO7$^{-/-}$ cells comparing day 12 of differentiation to day 0. Individual clusters are displayed on Hotelling plots for each genotype.

EXPERIMENTAL MATERIALS AND METHODS

All details and catalogue numbers can be found in the **Materials Table (Supplemental Table S9).** Protocols associated with this work can be found on protocols.io (dx.doi.org/10.17504/protocols.io.kxygx99pwg8j/v1)

Cloning and plasmid generation

The construction of lentiviral expression constructs used in this study have been previously described: pHAGE-mt-mKeima in (Heo *et al.*, 2015), PB-mt-mKeimaXL (Ordureau *et al.*, 2021) and pHAGE-GFP-Parkin in (Ordureau *et al.*, 2018).

Cell culture, generation of lentiviral stable cell lines.

HeLa Flip-In T-Rex (HFT) expressing doxycycline-inducible WT-Parkin (HeLa HFT/TO-PRKN-WT) cells (Heo *et al.*, 2015) and HEK293T were maintained in Dulbecco's modified Eagles medium (DMEM), supplemented with 10% vol/vol fetal bovine serum (FBS), 5% vol/vol penicillin-streptomycin (P/S), 5% vol/vol GlutaMAX and 5% vol/vol Non-essential amino acids (NEAA) at 37°C, 5% O_2.

Stable cell lines were generated using lentivirus generated from HEK293T cells. pHAGE-mt-mKeima or pHAGE-eGFP-Parkin were co-transfected in HEK293T cells together with the lentiviral vectors pSpax2 and pMD2.1 using Lipofectaime LTX reagent (Thermo Fisher Scientific, 15338100), according to manufacturer's instructions. Virus was harvested, filtered (0.45 µm) and added 8µg/ml polybrene and target cells infected for 18 h. Antibiotic selection was performed using 1 µg/ml puromycin or FACS sorting and cells verified using immunoblotting or fluorescence microscopy.

If not stated otherwise, Parkin expression in HeLa HFT/TO-PRKN was induced using 2 µg/ml doxycycline o/n, and subsequent mitophagy induced using Antimycin A / Oligomycin A (==AO) for the indicated times.

H9 ES cells harboring the mitochondrial mt-mKeima flux reporter (Ordureau *et al.*, 2020) were generated by electroporation of $1x10^6$ cells with 2.5 µg of pAC150-PiggyBac-matrix-mKeima^{XL} along with 2.5 µg of pCMV-HypBAC-PiggyBac-Helper, as described (Ordureau *et al.*, 2020). The cells were selected and maintained in E8 medium supplemented with 50 µg/ml Hygromycin and Hygromycin was kept in the medium during differentiation to iNeurons.

Gene-Editing and iNeuron differentiation

Generation of HeLa HFT cells lacking FBXO7$^{-/-}$ was facilitated using CRISPR/Cas9 with target sites determined using CHOPCHOP (Labun *et al*, 2019). Guide RNAs were ligated into the px459 plasmid (Addgene plasmid # 62988) and cells transfected using Lipofectaime LTX reagent (Thermo Fisher Scientific, 15338100), according to manufacturer's instructions. Two days post-transfection, single GFP positive cells were sorted into 96-well dishes containing 300µl full growth medium (composition as described above). Single cells were allowed to grow into colonies, then duplicated for MiSeq analysis and maintenance. Knockout candidates were confirmed by Western blot on whole cell lysates. The sgRNAs were generated using *GeneArt Precision gRNA Synthesis Kit* (Thermo Fisher Scientific) according to the manufacturer's instruction and purified using RNeasy Mini Kit (Qiagen). The sgRNA target sequence: ACCGATTCACTACAGAGCAT.

The PINK1$^{-/-}$ H9 cells used here, wherein sequences in exon 1 were deleted using CRISPR-Cas9 to create a null allele, were reported previously (Ordureau *et al.*, 2018). To generate FBXO7$^{-/-}$ H9 ES or HeLa cells, 0.6 µg sgRNA was incubated with 3 µg SpCas9 protein for 10 minutes at room temperature and electroporated into $2x10^5$ WT H9 cells using Neon transfection system (Thermo Fisher Scientific). Mutants were identified by Illumina MiSeq and further confirmed by Western blotting. For introduction of TRE3G-NGN2 into the AAVS1 site, a donor plasmid pAAVS1-TRE3G-NGN2 was generated by replacing the EGFP sequence with N-terminal flag-tagged human NGN2 cDNA sequence in plasmid pAAVS1-TRE3G-EGFP (Addgene plasmid # 52343). Five micrograms of pAAVS1-TRE3G-NGN2, 2.5 µg hCas9 (Addgene plasmid # 41815), and 2.5 µg gRNA_AAVS1-T2 (Addgene plasmid #

714 41818) were electroporated into $1x10^6$ H9 cells. The cells were treated with 0.25 µg/ml
715 Puromycin for 7 days and surviving colonies were expanded and subjected to genotyping.
716 Human ES cells (H9, WiCell Institute) were cultured in E8 medium (Chen *et al*, 2011)
717 on Matrigel-coated tissue culture plates with daily medium change. Cells were passaged
718 every 4-5 days with 0.5 mM EDTA in 1× DPBS (Thermo Fisher Scientific). SpCas9 and
719 AsCas12a/AsCpf1 expression plasmids pET-NLS-Cas9-6xHis (Addgene plasmid # 62934)
720 and modified pDEST-his-AsCpf1-EC, generated by deleting the MBP sequence from
721 plasmid pDEST-hisMBP-AsCpf1-EC (Addgene plasmid # 79007), were transformed into
722 *Rosetta™(DE3)pLysS* Competent Cells (Novagen), respectively, for expression. SpCas9
723 and AsCas12a/AsCpf1 proteins were purified as described elsewhere (Hur *et al*, 2016; Zuris
724 *et al*, 2015). Briefly, cells expressing SpCas9 [0.5 mM isopropylthio-β-galactoside, 14-hour
725 induction] were lysed in FastBreak buffer (Promega, Inc) and the NaCl concentration
726 adjusted to 500 mM. Extracts were centrifuged at 38,000g for 10 min at 4°C and the
727 supernatant incubated with Ni-NTA resin for 1 hour. The resin was washed extensively with
728 50 mM Tris pH8.0, 500 mM NaCl, 10% glycerol, 20 mM imidazole, and 2 mM TCEP prior to
729 elution with this buffer supplemented with 400 mM imidazole. Proteins were diluted two
730 volumes/volume in PBS and fractionated on a Heparin-Sepharose column using a 0.1 to 1.0
731 M NaCl gradient. Cas9-containing fractions were stored in PBS, 20% glycerol, 2 mM TCEP
732 at -80°C. AsCpf1 expression was induced similarly, and cells pelleted by centrifugation. Cells
733 were lysed by sonication in 50 mM HEPES pH7, 200 mM NaCl, 5 mM $MgCl_2$, 1 mM DTT,
734 and 10 mM imidazole supplemented with lysozyme (1 mg/ml) and protease inhibitors (Roche
735 complete, EDTA-free). After centrifugation (16,000g for 30 min), the supernatant was
736 incubated with Ni-NTA resin, the resin washed with 2M NaCl, and bound proteins eluted with
737 250 mM imidazole, and buffer exchanged into lysis buffer lacking $MgCl_2$ and imidazole prior
738 to storage at -80°C.
739 For human ES cell conversion to iNeurons, cells were expanded and plated at
740 $2x10^4/cm^2$ on Matrigel-coated tissue plates in DMEM/F12 supplemented with 1x N2, 1x
741 NEAA (Thermo Fisher Scientific), human Brain-derived neurotrophic factor (BDNF, 10 ng/ml,
742 PeproTech), human Neurotrophin-3 (NT-3, 10 ng/ml, PeproTech), mouse laminin (0.2 µg/ml,
743 Cultrex), Y-27632 (10 µM, PeproTech) and Doxycycline (2 µg/ml, Alfa Aesar) on Day 0. On
744 Day 1, Y-27632 was withdrawn. On Day 2, medium was replaced with Neurobasal medium
745 supplemented with 1x B27 and 1x Glutamax (Thermo Fisher Scientific) containing BDNF,
746 NT-3 and 1 µg/ml Doxycycline. Starting on Day 4, half of the medium was replaced every
747 other day thereafter. On Day 7, the cells were treated with Accutase (Thermo Fisher
748 Scientific) and plated at $3\text{-}4x10^4/cm^2$ on Matrigel-coated tissue plates. Doxycycline was
749 withdrawn on Day 10.
750
751 *Immunoblotting*
752 At the indicated times, ES cells, iNeurons or HeLa cells were washed on ice in 1x PBS,
753 harvested and pellet wash with 1x PBS and resuspended in 8 M urea buffer (8 M urea, 150
754 mM TRIS pH 7.4, 50 mM NaCl, PhosSTOP phosphatase inhibitor cocktail). Resuspended
755 cell lysates were sonicated for 10 seconds and debris pelleted at 13,000 rpm for 10 min.
756 Protein concentration was determined by BCA assay according to manufacturer's
757 instructions (Thermo Fisher Scientific, 23227). Indicated amounts of proteins were
758 resuspended in 1xLDS + 100 mM DTT and boiled for 10 minutes at 85°C. Equal amount of
759 protein and volume were loaded run on 4%-20% Bis-Tris, 8% Tris NuPAGE gels for 5
760 minutes at 100V, 5 min at 150 V and then run at 200 V for the required time. Gels were
761 transferred via wet transfer system onto PDVF membranes for immunoblotting.
762 Chemiluminescence and colorimetric images were acquired using a BioRad ChemiDoc MP
763 imaging system. Images from Western Blots were exported and analysed using Image Lab
764 and ImageJ/FiJi (Schindelin *et al*, 2012).
765
766
767
768

769
770
771 *PROTEOMICS*
772 *Proteomics – general sample preparation*
773 Sample preparation of proteomic analysis of whole-cell extract from HeLa, hESC, NPC and
774 iNeurons was performed according to previously published studies (Ordureau *et al.*, 2021;
775 Ordureau *et al.*, 2020). Cells were harvested on ice and plates were washed twice with 1x
776 PBS and detached in 1x PBS using cell scraper. After pelleting at 2000 rpm for 5 min at 4°C,
777 cells were washed 2x with 1x PBS and resuspended in 8 M urea buffer (composition stated
778 above). After sonification for 10 seconds, resuspended cells were pelleted for 10 min at
779 13000 rpm. Protein concentration was determined using BCA kit (Thermo Fisher Scientific,
780 23227).
781 Unless otherwise noted, proteomics and data analysis was performed as described
782 (Ordureau *et al.*, 2021; Ordureau *et al.*, 2020). Briefly, protein extracts (100 µg) were
783 subjected to disulfide bond reduction with 5 mM TCEP (room temperature, 10 min) and
784 alkylation with 25 mM chloroacetamide (room temperature, 20 min). Methanol–chloroform
785 precipitation was performed prior to protease digestion. In brief, four parts of neat methanol
786 were added to each sample and vortexed, one part chloroform was then added to the
787 sample and vortexed, and finally three parts water was added to the sample and vortexed.
788 The sample was centrifuged at 6,000 rpm for 2 min at room temperature and subsequently
789 washed twice with 100% methanol. Samples were resuspended in 100 mM EPPS pH8.5
790 containing 0.1% RapiGest and digested at 37 °C for 8h with Trypsin at a 100:1 protein-to-
791 protease ratio. Samples were acidified with 1% Formic Acid for 15 min and subjected to C18
792 solid-phase extraction (SPE) (Sep-Pak, Waters).
793
794 *Proteomics – quantitative proteomics using TMT*
795 Tandem mass tag labeling of each sample (50 mg peptide input) was performed by adding 5
796 uL of the 25 ng/mL stock of TMTpro reagent along with acetonitrile to achieve a final
797 acetonitrile concentration of approximately 30% (v/v). Following incubation at room
798 temperature for 1 h, the reaction was quenched with hydroxylamine to a final concentration
799 of 0.5% (v/v) for 15 min. The TMTpro- labeled samples were pooled together at a 1:1 ratio.
800 The sample was vacuum centrifuged to near dryness, and following reconstitution in 1% FA,
801 samples were desalted using C18 solid-phase extraction (SPE) (50 mg, Sep-Pak, Waters),
802 according to manufacturer protocol.
803 Dried TMTpro-labeled peptides (~300 ug) were resuspended in 10 mM NH_4HCO_3 pH
804 8.0 and fractionated using basic pH reverse phase HPLC (Wang *et al*, 2011). Briefly,
805 samples were offline fractionated over a 90 min run, into 96 fractions by high pH reverse-
806 phase HPLC (Agilent LC1260) through an Aeris peptide xb-c18 column (Phenomenex; 250
807 mm x 3.6 mm) with mobile phase A containing 5 % acetonitrile and 10 mM NH_4HCO_3 in LC-
808 MS grade H_2O, and mobile phase B containing 90 % acetonitrile and 10 mM NH_4HCO_3 in
809 LC-MS grade H_2O (both pH 8.0). The 96 resulting fractions were then pooled in a non-
810 continuous manner into 24 fractions (as outlined in Figure S5 of (Paulo *et al*, 2016)) and sets
811 of 12 fractions (even or odd numbers) were used for subsequent mass spectrometry
812 analysis. Fractions were vacuum centrifuged to near dryness. Each consolidated fraction
813 was desalted via StageTip, dried again via vacuum centrifugation, and reconstituted in 5 %
814 acetonitrile, 1 % formic acid for LC-MS/MS processing.
815 TMT proteomics samples were subjected to analysis using a Orbitrap Fusion Lumos
816 Tribrid mass spectrometer (Thermo Fisher Scientific, San Jose, CA) online with Proxeon
817 EASY-nLC1200 liquid chromatography (Thermo Scientific). Peptides were resuspended in 5
818 % ACN/5 % FA and 10 % of the samples were loaded on a 35 cm analytical column (100mm
819 inner diameter) packed in-house with Accurcore150 resin (150 Å, 2.6 mm, Thermo Fisher
820 Scientific, San Jose, CA) for LC-MS analysis. Peptide separation was performed with a
821 gradient of acetonitrile (ACN, 0.1% FA) from 3-13 % (0-83 min) and 13-28 % (80-83 min)
822 during a 90 min run.

For the HeLa TMTpro proteomic samples, LC-hrMS/MS was combined with 3 optimized CV parameters on the FAIMS Pro Interface to reduced precursor ion interference (Schweppe *et al*, 2019). Data-dependent acquisition (DDA) was performed by selecting the most abundant precursors from each CV's (-40/-60/-80) MS^1 scans for hrMS/MS over a 1-1.5s duty cycle (1s/1.5s/1s respectively). The MS^1 scan parameters include a 400-1,600 m/z mass range at 60,000 resolution (at 200 Th) with 4 x 10^5 automated gain control (AGC) (100 %), and a maximum injection time (max IT) of 50 ms. Precursors (z=2-5) were isolated with 0.7 Th (quadrupole), fragmented with high energy C-trap dissociation (HCD) at 36 normalized collision energy (NCE), and subjected to hrMS/MS on the Orbitrap at 50,000 resolution (at 200 Th), 120 ms max IT, fixed first mass 110 Th, and 1.0 x 10^5 AGC (200%). Precursors were placed on 90 s dynamic exclusion (+/- 10 ppm) to prevent redundant sampling.

In the iNeuron TMTpro experiments, the same FAIMS and MS^1 parameters were implemented (with 1.25 s duty cycle/CV for DDA) with the Multi-Notch SPS-MS3 acquisition method (McAlister *et al*, 2014), to further reduce ion interference in TMT reporter quantification (Paulo *et al.*, 2016). Most abundant precursors (with 120 s dynamic exclusion +/- 10 ppm) were selected from MS^1 scans, isolated using the quadrupole (0.6 Th isolation), fragmented with collision-induced dissociation (CID) at 35 NCE, and subjected to MS/MS in the ion trap (turbo scan speed, 35 ms max IT, 1.0 x 10^4 AGC). Using Real Time Search analysis software (Erickson *et al*, 2019; Schweppe *et al*, 2020), a synchronous-precursor-selection (SPS) API-MS^3 scan was collected on the top 10 most intense b- or y-ions from the matched peptide identification (determined by an online search of its respective MS/MS scan). MS^3 scans were performed on the Orbitrap (AGC 2.0 x 10^5; NCE 55; max IT 250 ms, 50,000 resolution at 200 Th). To increase quantitative sampling (MS^3 scans) of proteins during each mass spectrometry injection, a 2 peptide per protein per sample closeout was set. This ensures no more than two peptide-spectrum matches per protein (that pass quality filters) are subjected to MS^3 scans, reducing redundant protein MS sampling and potentially increasing proteome depth (Schweppe *et al.*, 2020).

Proteomics Data Analysis

Mass spectrometry raw data were converted to mzXML and monoisotopic peaks were reassigned using Monocle (Rad *et al*, 2021). Mass spectra were database searched using Sequest algorithm (2019.01 rev. 5; (Eng *et al*, 1994)) against the Human Reference Proteome Uniprot database (2019-01 SwissProt entries only; UniProt Constortium, 2015) appended with sequences of common contaminates and reverse sequences of proteins as decoys, for target-decoy competition (Elias & Gygi, 2007). Sequest search parameters include: 50 ppm precursor tolerance, 0.9 Da product ion tolerance, trypsin endopeptidase specificity (C-terminal to [KR], 2 max missed cleavages), static modifications on peptide N-terminus and lysines with TMTpro tags (+304.207 Da) and carbamidomethylation on cysteines (57.021 Da), and variable modification of oxidation on methionines (+15.995 Da). Peptide-spectrum matches were filtered at 2% false discovery rate (FDR) using linear discriminant analysis (Huttlin *et al*, 2010), based on XCorr, DeltaCn, missed cleavages, peptide length, precursor mass accurracy, fraction of matched product ions, charge state, and number of modifications per peptide (additionally restricting PSM Xcorr >1 and peptide length>6). Following a 2% protein FDR filter (Savitski *et al*, 2015), PSMs reporter ion intensities were quantified (most intense centroid within 0.003 Da of theoretical TMT reporter mass), filtered based on a precursor isolation specificity > 0.5, and filtered by a summed signal-to-noise across TMT channels > 100.

Protein quantification was performed via the summation (weighted average) of its constituent PSMs' reporter intensities and TMT channels were normalized for protein input to total TMT channel intensity across all quantified PSMs (adjusted to median total TMT intensity for the TMT channels) (Plubell *et al*, 2017). Log_2 normalized summed protein reporter intensities were compared using a Student's t-test and p-values were corrected for multiple hypotheses using the Benjamini-Hochberg adjustment (Benjamini & Hochberg, 1995). Resultant q-values and mean log_2 fold changes between conditions were used to

878 generate volcano plots. Hotelling T^2 analysis was performed using the normalized summed
879 protein reporter ion intensities and the timecourse (v. 1.66.0; (Tai, 2022)) package in R.
880 The annotation list for the subcellular localization of organellar protein markers was
881 derived from previously published high confidence HeLa dataset ((Itzhak *et al*, 2016); "high"
882 & "very high" confidence) and additional manual entries (Ordureau *et al.*, 2021). MitoCharta
883 3.0 (Rath *et al*, 2021) was used for mitochondrial annotation, whereas annotations for
884 ribosome and autophagy components were used from previous studies (An *et al*, 2020).
885 Transcription factor and neuronal development markers were based on previously published
886 databases and publications (Lambert *et al*, 2018; Ordureau *et al.*, 2021). Figures were
887 generated using a combination of Excel, R (v.4.2.0) in RStudio (2022.07.01 Build 554),
888 Perseus (v1.6.5 (Tyanova & Cox, 2018)), GraphPad Prism (v9.1.0), and Adobe Illustrator
889 (26.2.1).
890
891 The **Supplemental Data Table S3-8** contains the quantified proteins as well as associated
892 TMT reporter ratio to control channels used for quantitative analysis.
893
894 *Interaction Proteomic Analysis*
895 For interaction analysis of FBXO7 and PINK1, interaction proteomics data from the Bioplex
896 Interactome (Huttlin *et al.*, 2021) was extracted for HEK293T and HCT116 samples
897 (**Supplemental Table S1,2**). The number of replicates in which a peptide-spectral match
898 (PSM) mapped to PINK1's or FBXO7's the Bioplex 3.0 interactomes was plotted via a
899 network diagram in R. (packages to add from R include (igraph 1.3.1, tidygraph 1.2.1, and
900 ggraph 2.0.5).
901
902 *MICROSCOPY*
903 Macros and pipelines used in this work can be found on GitHub
904 (https://github.com/harperlaboratory/FBXO7.git) or
905 Zenodo (https://doi.org/10.5281/zenodo.7258918).
906
907 *Live-cell confocal microscopy for mitophagic flux analysis over differentiation (mt-mKeima^{XL})*
908 For quantitative Keima-flux analysis (Ordureau *et al.*, 2020), hESC were seeded on day 4 of
909 differentiation into 6-well 1.5 high performance glass bottom plates (Cellvis, P06-1.5H-N)
910 and further differentiated in the vessel for the indicated times until reaching appropriate
911 confluency and imaged. iNeurons were imaged using a Yokogawa CSU-W1 spinning disk
912 confocal on a Nikon Eclipse Ti-E motorized microscope. The system is equipped with a
913 Tokai Hit stage top incubator and imaging was performed at 37°C, 5% CO_2 and 95%
914 humidity under a Nikon Plan Apo 60×/1.40 N.A immersion oil objective lens. For ratiometic
915 imaging, mtKeimaXL were excited in sequential manner with a Nikon LUN-F XL solid state
916 laser combiner ([laser line – laser power]: 445 - 80mW, 561 - 65mW]) using a
917 Semrock Di01-T445/515/561 dichroic mirror. Fluorescence emissions were collected
918 through a Chroma ET605/52m [for 445 nm] and a 568 Chroma ET605/52m [for 561 nm],
919 filters, respectively (Chroma Technologies). Confocal images were acquired with a
920 Hamamatsu ORCA-Fusion BT CMOS camera (6.5 μm^2 photodiode, 16-bit) camera and NIS-
921 Elements image acquisition software. Consistent laser intensity and exposure time were
922 applied to all the samples, and brightness and contrast were adjusted equally by applying
923 the same minimum and maximum display values in ImageJ/FiJi (Schindelin *et al.*, 2012).
924 Image quantification was performed in ImageJ/FiJi using custom-written batch-macros.
925 In brief, raw confocal images of mitochondrial targeted mt-mKeima^{XL} were divided
926 [ex:561/ex:445] resulting in a ratiometic image of only acidic Keima-puncta. These signals
927 were subjected to background subtraction (rolling kernel size 25, sliding paraboloid) and
928 converted to binary objects. The "Analyze Particles..." command (pixel size exclusion: 0.5-∞,
929 exclude edge objects) was used to measure foci-abundance and other morphological
930 parameters. Results for each image-stack saved as .csv files, together with the original
931 ratiometic .tiff file for QC purposes. Unless stated otherwise all images represent z-

932 projections. Statistical analysis and plotting of microscopy data was performed in Prism
933 (v9.1.0, GraphPad).
934
935
936
937
938 *Immunocytochemical analysis*
939 iNeurons or HeLa cells were fixed with warm 4% paraformaldehyde (Electron Microscopy
940 Science, #15710, purified, EM grade) in PBS at 37°C for 30 min and permeabilized with
941 0.5% Triton X-100 in PBS for 15 minutes at room temperature. After three washes with
942 0.02% Tween20 in PBS (PBST), cells were blocked for 10 min in 3% BSA-1xPBS at room
943 temperature and washed again three times in PBST. Cells were incubated for 3h in primary
944 antibodies in 3% BSA-1xPBS and washed three times with PBST. Secondary antibodies
945 (Thermo Scientific, 1:400 in 3% BSA-1xPBS) where applied for 1h at room temperature.
946 Alexa Fluor 633 Phalloidin (Thermo Fisher, 1:200, A22284) was added with secondary
947 antibodies to label F-actin. To stain nuclei, Hoechst33342 (1:10000) was added for 5 min to
948 cells in PBST and final three washes performed before mounting in Vectashield (Vector
949 Laboratories, H-1000-10). Primary and secondary antibodies used in this study can be found
950 in the **Materials Table (Supplemental Table S9).**
951
952 *Fixed-cell microscopy – general acquisition parameters*
953 Immunofluorescently labelled Hela or iNeurons (antibodies indicated in figures and figure
954 legends and details in **Materials Table, (Supplemental Table S9)**) were imaged at room
955 temperature using a Yokogawa CSU-W1 spinning disk confocal on a Nikon Eclipse Ti-E
956 motorized microscope equipped with a Nikon Plan Apochromat 40×/0.40 N.A air-objective
957 lens, Nikon Apochromat 60×/1.42 N.A oil-objective lens and a Plan Apochromat 100×/1.45
958 N.A oil-objective lens. Signals of 405/488/568/647 fluorophores were excited in sequential
959 manner with a Nikon LUN-F XL solid state laser combiner ([laser line – laser power]: 405 -
960 80mW, 488 - 80mW, 561 - 65mW, 640nm - 60mW]) using a Semrock Di01-
961 T405/488/568/647 dichroic mirror. Fluorescence emissions were collected with
962 Chroma ET455/50m [405 nm], 488 Chroma ET525/50m [488 nm], 568 Chroma ET605/52m
963 [561 nm], 633 Chroma ET705/72m [640 nm] filters, respectively (Chroma Technologies).
964 Confocal images were acquired with a Hamamatsu ORCA-Fusion BT CMOS camera (6.5
965 μm^2 photodiode, 16-bit) camera and NIS-Elements image acquisition software. Consistent
966 laser intensity and exposure time were applied to all the samples, and brightness and
967 contrast were adjusted equally by applying the same minimum and maximum display values
968 in ImageJ/FiJi (Schindelin *et al.*, 2012).
969
970 *Microscopy-based mitochondrial morphology measurements in iNeurons*
971 For quantitative measurement of mitochondrial morphology in d12 iNeurons under fed or
972 mitophagy conditions, HeLa cells were seeded on 6-well 1.5 high performance glass bottom
973 plates (Cellvis, P06-1.5H-N) and mitophagy induced for the indicated time durations.
974 Alternatively, hESC were seeded on day 4 of differentiation into 6-well 1.5 high performance
975 glass bottom plates (Cellvis, P06-1.5H-N) and differentiated in the vessel into iNeurons and
976 mitophagy induced for the indicated time durations. Cells were fixed and stained as
977 described above. Z-stacks were acquired with a Nikon Plan Apo 100×/1.45 N.A oil-objective
978 lens and with the parameters stated above. Image quantification was performed in
979 ImageJ/FiJi using custom-written batch-macros.
980 Statistical analysis and plotting of microscopy data was performed in Prism (v9.1.0,
981 GraphPad). Primary and secondary antibodies used in this study can be found in the
982 **Materials Table (Supplemental Table 9)**.
983
984 *Microscopy-based mtDNA turnover measurements in HeLa and iNeurons*
985 For quantitative measurement of mtDNA turnover after AO-induced mitophagy, HeLa cells
986 were seeded on 6-well 1.5 high performance glass bottom plates (Cellvis, P06-1.5H-N) and

987 mitophagy induced for the indicated time durations. Alternatively, hESC were seeded on day
988 4 of differentiation into 6-well 1.5 high performance glass bottom plates (Cellvis, P06-1.5H-
989 N) and differentiated in the vessel into iNeurons and mitophagy induced for the indicated
990 time durations. Cells were fixed and stained as described above, but primary antibody
991 incubation with aDNA (1:200) was performed overnight. Z-stacks were acquired with a Nikon
992 Plan Apo 100×/1.45 N.A oil-objective lens and with the parameters stated above. Image
993 quantification was performed in ImageJ/FiJi using custom-written batch-macros. In brief,
994 both aDNA and nuclear signals were converted to binary files and the nuclear signal
995 subtracted from the aDNA signal, resulting in an image stack containing only the mtDNA
996 intensities. The "Analyze Particles..." command (pixel size exclusion: 0.05-3, exclude edge
997 objects) was used to measure morphological features and results for each image-stack
998 saved as .csv files, together with the analyzed binary-mask overlay .tiff file for QC purposes.
999 Number of mtDNA signals were normalized to cell number found in the same image stack.
1000 Statistical analysis and plotting of microscopy data was performed in Prism (v9.1.0,
1001 GraphPad). Primary and secondary antibodies used in this study can be found in the
1002 **Materials Table (Supplemental Table S9)**.
1003
1004 *Microscopy-based measurements of p62 recruitment in HeLa*
1005 For quantitative measurement of p62 recruitment to mitochondria, HeLa control and
1006 knockout cells were seed in 1.5 high performance glass bottom plates and doxycycline
1007 added over night to induce Parkin expression. Mitophagy was induced using Oligomycin A /
1008 Antimycin A for 16h in full DMEM in presence of doxycycline. Cells were fixed and stained
1009 as stated above and imaged using a Nikon Plan Apo 60×/1.42 N.A air-objective lens and
1010 with the parameters stated above. 8 µM z-stacks were taken for each selected field of view.
1011 Image quantification was performed in ImageJ/FiJi using custom-written batch-
1012 macros. The p62 channel was filtered (Gaussian Blue, sigma =2) and converted into binary
1013 files using the Intermodes thresholding method. p62 spots were counted using the “Analyze
1014 Particles...” function (pizel size exclusion: 0.1-30, exclude edge objects) and results for each
1015 image-stack saved as .csv files, together with the analyzed binary-mask overlay .tiff file for
1016 QC purposes. The DAPI channel was used to count nuclei for per cell normalization.
1017 Statistical analysis and plotting of microscopy data was performed in Prism (v9.1.0,
1018 GraphPad). Primary and secondary antibodies used in this study can be found in the
1019 **Materials Table (Supplemental Table S9).**
1020
1021 *Microscopy-based pUb-coverage measurements of mitochondria in iNeurons*
1022 For quantitative measurement of pUb coverage over mitochondria AO-induced mitophagy,
1023 hESC were seeded on day 4 of differentiation into 6-well 1.5 high performance glass bottom
1024 plates (Cellvis, P06-1.5H-N) and differentiated in the vessel into iNeurons and mitophagy
1025 induced for the indicated time durations. Cells were fixed and stained as described above,
1026 using anti-HSP60 to label mitochondria and anti-pUb (Ser65) to label pUb. 3-5 10 µm thick
1027 z-stacks per replicate per sample were acquired using a Nikon Plan Apo 60×/1.42 N.A air-
1028 objective lens and with the parameters stated above.
1029 Image quantification was performed in ImageJ/FiJi using custom-written batch-
1030 macros. In brief, mitochondrial signal was filtered (Gaussian Blur, sigma=2), converted into
1031 binary files and holes in the resulting mask filled. pUb channel was thresholded into a binary
1032 file (Triangle method); these masks were measured using the "Analyze Particles..."
1033 command (pixel size exclusion: 0.5-∞, exclude edge objects) and results for each image-
1034 stack saved as .csv files, together with the analyzed binary-mask overlay .tiff file for QC
1035 purposes. % of mitochondrial pUb coverage was calculated and normalized to [t]=6h AO.
1036 Statistical analysis and plotting of microscopy data was performed in Prism (v9.1.0,
1037 GraphPad). Primary and secondary antibodies used in this study can be found in the
1038 **Materials Table (Supplemental Table S9).**
1039
1040 *Microscopy-based evaluation of Parkin translocation and mitophagy in FBXO7$^{-/-}$ cell lines*

1041 For quantitative measurement of Parkin translocation kinetics in FBXO7$^{-/-}$ cell lines, stable
1042 HeLa cell lines expressing GFP-Parkin were created. WT and knockout cell lines were
1043 seeded into 12-well 1.5 high performance glass bottom plates (Cellvis, P12-1.5H-N) two
1044 days prior to experimental manipulation. Mitophagy was induced as described above using
1045 Antimycin A / Oligomycin A for 1h. Treated and control (fed) cells were fixed as described
1046 above, stained for mitochondria (HSP60), Parkin (GFP) and DNA (SpyDNA-555) and 8µm z-
1047 stacks were acquired with a Nikon Plan Apo 60×/1.42 N.A oil-objective lens and with the
1048 parameters stated above. For quantitate single-cell analysis, a total of ~240 randomly xy-
1049 marked stacks were acquired, and MIPs used for subsequent analysis. CellProfiler (Stirling
1050 *et al.*, 2021) was used for the quantitative analysis of single-cells and mitochondrial objects
1051 (segmentation and analysis pipelines can be found on GitHub). Plotting of microscopy data
1052 was performed in Prism (v9.1.0, GraphPad) and R using the following libraries: tidyverse,
1053 dplyr, tibble, viridis, ggplot2, ggridges, ggsci. Primary and secondary antibodies used in this
1054 study can be found in the **Materials Table (Supplemental Table S9)**.
1055
1056 *Immunocytochemical sample preparation for 3D-SIM*
1057 Sample preparation and SIM acquisition guidelines from (Kraus *et al*, 2017) were used as a
1058 basis for the super-resolution analysis of pUb spreading after mitophagy induction. iNeurons
1059 or HeLa cells were seeded on 18x18 mm Marienfeld Precision cover glasses thickness No.
1060 1.5H (tol. ± 5 µm). Cover glasses were coated, if necessary, for hESC / iNeuron culture as
1061 described above. After experimental manipulation, cells were fixed with warm
1062 paraformaldehyde 3% Glutaraldehyde 0.35% in 0.1M Sodium Cacodylate, pH 7.4 (Electron
1063 Microscopy Science) at 37°C for 30 min and permeabilized with 0.5% Triton X-100 in PBS
1064 for 15 minutes at room temperature. After three washes with 0.02% Tween20 in PBS
1065 (PBST), cells were blocked for 10 min in 3% BSA-1xPBS at room temperature and washed
1066 again three times in PBST. iNeurons were incubated overnight in primary antibodies in 3%
1067 BSA-1xPBS and washed three times with PBST. Secondary antibodies (Thermo Scientific,
1068 1:400 in 3% BSA-1xPBS) where applied for 1 h at room temperature. To stain nuclei, DAPI
1069 was added for 5 min to cells in PBST, washed three times for 5 min in 1xPBST before a
1070 post-fixation in 4% paraformaldehyde was performed. After 2 washes in PBST, coverslips
1071 were washed once in 1xPBS and mounted in Vectashield (Vector Laboratories, H-1000-10)
1072 on glass slides. Primary and secondary antibodies used in this study can be found in the
1073 **Materials Table (Supplemental Table S9)**.
1074
1075 *3D-SIM microscopy – acquisition parameters*
1076 3D-SIM microscopy was performed on a DeltaVision OMX v4 using an Olympus 60x / 1.42
1077 Plan Apo oil objective (Olympus, Japan). The instrument is equipped with 405 nm, 445 nm,
1078 488 nm, 514 nm, 568 nm and 642 nm laser lines (all >= 100 mW) and images were recorded
1079 on a front-illuminated sCMOS (PCO Photonics, USA) in 512x512px image size mode, 1x
1080 binning, 125 nm z-stepping and with 15 raw images taken per z-plane (5 phase-shifts, 3
1081 angles). Raw image data was computationally reconstructed using CUDA-accelerated 3D-
1082 SIM reconstruction code (https://github.com/scopetools/cudasirecon) based on (Gustafsson
1083 *et al*, 2008). Optimal optical transfer function (OTF) was determined via an in-house build
1084 software, developed by Talley Lambert from the NIC / CBMF (GitHub:
1085 https://github.com/tlambert03/otfsearch, all channels were registered to the 528nm output
1086 channel, Wiener filter: 0.002, background: 90).
1087
1088 *3D-SIM microscopy – pUb – mitochondria 3D renderings & analysis*
1089 3D renderings of 3D-SIM images were performed in UCSF Chimera X
1090 (https://www.cgl.ucsf.edu/chimerax/) using 32-bit .tiff image stacks. Image channels were
1091 sequentially imported and visualized as surfaces using the "Volume Viewer" tool. Surface
1092 representations were cleaned up using the "High dust" command, based on size filtering
1093 thresholding.
1094 3D-analysis of HeLa and iNeuron datasets from 3D-SIM datasets was performed
1095 using Imaris (Oxford Instruments, v9.7). After converting all multi-color .tiff to native .ims

1096 files, import into Imaris Arena and global background subtraction, mitochondrial and pUb
1097 objects were segmented from seeds (XY starting diameter: 0.08 µm == pixel size of images),
1098 segmented based on automatic thresholding with local background subtraction and splitting
1099 of touching objects (0.4µm). Objects were piped into Imaris Vantage module for further
1100 analysis. In Vantage, nearest neighbour distances of pUb to pUb and between pUb and
1101 mitochondria, as well as volume of segmented objects were computed. This pipeline was
1102 tested on WT control cells and then applied for batch processing on all other genotype to
1103 allow for unbiased segmentation and analysis. On average, 10 cells were analysed per
1104 genotype per condition (121 total) for HeLa cells, and 12 cells (139 total) for iNeurons.
1105 Unless stated otherwise, all images depicted in figures are maximum-intensity
1106 projections.
1107
1108 *Flow cytometry-based measurement of mitophagic flux*
1109 HeLa HFT/TO-PRKN cells of the indicated genotype (control, PINK1$^{-/-}$, FBXO7 $^{-/-}$) expressing
1110 mtKeima (Heo *et al.*, 2015) were seeded into 12-well dishes. Upon reaching 60%
1111 confluency, 2 µg/ml doxycycline was added to induce Parkin expression for at least eight
1112 hours before depolarization of mitochondria. Following Parkin induction, cells were treated
1113 with Antimycin A (0.5 µM) and Oligomycin (0.5 µM) for the indicated number of hours.
1114 Bafilomycin A (25 nM, Sigma-Aldrich, B1793)-treated samples were treated for three hours.
1115 Control cells were fed three hours before experimental manipulation. To harvest cells for
1116 analysis, each well was washed with 1 mL PBS then treated with 100 µL of 0.25% trypsin for
1117 3 min at room temperature, resuspended in 300 µL of DMEM with 10% FBS. 200 µL of each
1118 sample was transferred to a flat-bottom 96-well plate for analysis by flow cytometry.
1119 hESCs were seeded at day 4 into coated 6-well dishes and differentiated. At day 12,
1120 mitophagy was induced with Antimycin A (0.5 µM) and Oligomycin (0.5 µM) or Bafilomycin A
1121 (25 nM, Sigma-Aldrich, B1793) for the indicated number of hours. Control cells were fed 2h
1122 before experimental manipulation. Cells were dissociated from the wells using Accutase and
1123 resuspended in 600 µL ND2 medium + 10 µM Y27632 and filtered through a cell strainer cap
1124 tube (Corning, 352235).
1125 Analysis of a population of at least 10,000 cells was performed on an Attune NxT
1126 (Thermo Fisher Scientific) detecting neutral mtKeima signal with excitation at 445 nm and
1127 emission 603 nm with a 48 nm bandpass and acidic mtKeima with 561 nm excitation and
1128 emission 620 nm and a 15 nm band pass. mtKeima ratio was analysed as previously
1129 described (An & Harper, 2018). Briefly, acidic:neutral Keima ratios were measured by gating
1130 a population of well-behaved single cells using forward and side scatter, followed by
1131 calculation of acidic:neutral mtKeima ratio on a per-cell basis in FlowJo Software (FlowJo,
1132 LLC).
1133
1134 **QUANTIFICATION AND STATISTICAL ANALYSIS**
1135 Unless stated otherwise all quantitative experiments were performed in triplicate and
1136 average with S.E.M. or S.D. as indicated in legends reported.
1137
1138 **REFERENCES**
1139 Al Rawi S, Simpson L, McDonald NQ, Chernuha V, Elpeleg O, Zeviani M, Barker RA, Spiegel R,
1140 Laman H (2022) Study of an FBXO7 patient mutation reveals Fbxo7 and PI31 co-regulate
1141 proteasomes and mitochondria. *BioRxiv*
1142 An H, Harper JW (2018) Systematic analysis of ribophagy in human cells reveals bystander
1143 flux during selective autophagy. *Nat Cell Biol* 20: 135-143
1144 An H, Ordureau A, Korner M, Paulo JA, Harper JW (2020) Systematic quantitative analysis of
1145 ribosome inventory during nutrient stress. *Nature* 583: 303-309
1146 Antico O, Ordureau A, Stevens M, Singh F, Nirujogi RS, Gierlinski M, Barini E, Rickwood ML,
1147 Prescott A, Toth R *et al* (2021) Global ubiquitylation analysis of mitochondria in primary

1148 neurons identifies endogenous Parkin targets following activation of PINK1. *Sci Adv* 7:
1149 eabj0722
1150 Bader M, Benjamin S, Wapinski OL, Smith DM, Goldberg AL, Steller H (2011) A conserved F
1151 box regulatory complex controls proteasome activity in Drosophila. *Cell* 145: 371-382
1152 Benjamini Y, Hochberg Y (1995) Controlling the false discovery rate: a practical and powerful
1153 approach to multiple testing. *Journal of the Royal Statistical Society, Series B* 57: 289-300
1154 Bingol B, Tea JS, Phu L, Reichelt M, Bakalarski CE, Song Q, Foreman O, Kirkpatrick DS, Sheng
1155 M (2014) The mitochondrial deubiquitinase USP30 opposes parkin-mediated mitophagy.
1156 *Nature* 510: 370-375
1157 Burchell VS, Nelson DE, Sanchez-Martinez A, Delgado-Camprubi M, Ivatt RM, Pogson JH,
1158 Randle SJ, Wray S, Lewis PA, Houlden H *et al* (2013) The Parkinson's disease-linked proteins
1159 Fbxo7 and Parkin interact to mediate mitophagy. *Nat Neurosci* 16: 1257-1265
1160 Burman JL, Pickles S, Wang C, Sekine S, Vargas JNS, Zhang Z, Youle AM, Nezich CL, Wu X,
1161 Hammer JA *et al* (2017) Mitochondrial fission facilitates the selective mitophagy of protein
1162 aggregates. *J Cell Biol* 216: 3231-3247
1163 Chen G, Gulbranson DR, Hou Z, Bolin JM, Ruotti V, Probasco MD, Smuga-Otto K, Howden SE,
1164 Diol NR, Propson NE *et al* (2011) Chemically defined conditions for human iPSC derivation
1165 and culture. *Nat Methods* 8: 424-429
1166 Deutsch EW, Bandeira N, Sharma V, Perez-Riverol Y, Carver JJ, Kundu DJ, Garcia-Seisdedos
1167 D, Jarnuczak AF, Hewapathirana S, Pullman BS *et al* (2020) The ProteomeXchange
1168 consortium in 2020: enabling 'big data' approaches in proteomics. *Nucleic Acids Res* 48:
1169 D1145-D1152
1170 Di Fonzo A, Dekker MC, Montagna P, Baruzzi A, Yonova EH, Correia Guedes L, Szczerbinska
1171 A, Zhao T, Dubbel-Hulsman LO, Wouters CH *et al* (2009) FBXO7 mutations cause autosomal
1172 recessive, early-onset parkinsonian-pyramidal syndrome. *Neurology* 72: 240-245
1173 Dikic I, Elazar Z (2018) Mechanism and medical implications of mammalian autophagy. *Nat*
1174 *Rev Mol Cell Biol* 19: 349-364
1175 Elias JE, Gygi SP (2007) Target-decoy search strategy for increased confidence in large-scale
1176 protein identifications by mass spectrometry. *Nat Methods* 4: 207-214
1177 Eng JK, McCormack AL, Yates JR (1994) An approach to correlate tandem mass spectral data
1178 of peptides with amino acid sequences in a protein database. *J Am Soc Mass Spectrom* 5:
1179 976-989
1180 Erickson BK, Mintseris J, Schweppe DK, Navarrete-Perea J, Erickson AR, Nusinow DP, Paulo
1181 JA, Gygi SP (2019) Active Instrument Engagement Combined with a Real-Time Database
1182 Search for Improved Performance of Sample Multiplexing Workflows. *J Proteome Res* 18:
1183 1299-1306
1184 Evans CS, Holzbaur EL (2020) Degradation of engulfed mitochondria is rate-limiting in
1185 Optineurin-mediated mitophagy in neurons. *Elife* 9
1186 Gladkova C, Maslen SL, Skehel JM, Komander D (2018) Mechanism of parkin activation by
1187 PINK1. *Nature* 559: 410-414
1188 Goodall EA, Kraus F, Harper JW (2022) Mechanisms underlying ubiquitin-driven selective
1189 mitochondrial and bacterial autophagy. *Mol Cell* 82: 1501-1513
1190 Gustafsson MG, Shao L, Carlton PM, Wang CJ, Golubovskaya IN, Cande WZ, Agard DA, Sedat
1191 JW (2008) Three-dimensional resolution doubling in wide-field fluorescence microscopy by
1192 structured illumination. *Biophys J* 94: 4957-4970
1193 Harper JW, Ordureau A, Heo JM (2018) Building and decoding ubiquitin chains for
1194 mitophagy. *Nat Rev Mol Cell Biol* 19: 93-108

1195 Heo JM, Ordureau A, Paulo JA, Rinehart J, Harper JW (2015) The PINK1-PARKIN
1196 Mitochondrial Ubiquitylation Pathway Drives a Program of OPTN/NDP52 Recruitment and
1197 TBK1 Activation to Promote Mitophagy. *Mol Cell* 60: 7-20
1198 Houlden H, Singleton AB (2012) The genetics and neuropathology of Parkinson's disease.
1199 *Acta Neuropathol* 124: 325-338
1200 Huang T, Fang L, He R, Weng H, Chen X, Ye Q, Qu D (2020) Fbxo7 and Pink1 play a reciprocal
1201 role in regulating their protein levels. *Aging (Albany NY)* 13: 77-88
1202 Hur JK, Kim K, Been KW, Baek G, Ye S, Hur JW, Ryu SM, Lee YS, Kim JS (2016) Targeted
1203 mutagenesis in mice by electroporation of Cpf1 ribonucleoproteins. *Nat Biotechnol* 34: 807-
1204 808
1205 Huttlin EL, Bruckner RJ, Navarrete-Perea J, Cannon JR, Baltier K, Gebreab F, Gygi MP,
1206 Thornock A, Zarraga G, Tam S *et al* (2021) Dual proteome-scale networks reveal cell-specific
1207 remodeling of the human interactome. *Cell* 184: 3022-3040 e3028
1208 Huttlin EL, Jedrychowski MP, Elias JE, Goswami T, Rad R, Beausoleil SA, Villen J, Haas W,
1209 Sowa ME, Gygi SP (2010) A tissue-specific atlas of mouse protein phosphorylation and
1210 expression. *Cell* 143: 1174-1189
1211 Itzhak DN, Tyanova S, Cox J, Borner GH (2016) Global, quantitative and dynamic mapping of
1212 protein subcellular localization. *Elife* 5
1213 Jin J, Cardozo T, Lovering RC, Elledge SJ, Pagano M, Harper JW (2004) Systematic analysis
1214 and nomenclature of mammalian F-box proteins. *Genes Dev* 18: 2573-2580
1215 Jin SM, Lazarou M, Wang C, Kane LA, Narendra DP, Youle RJ (2010) Mitochondrial
1216 membrane potential regulates PINK1 import and proteolytic destabilization by PARL. *J Cell*
1217 *Biol* 191: 933-942
1218 Kane LA, Lazarou M, Fogel AI, Li Y, Yamano K, Sarraf SA, Banerjee S, Youle RJ (2014) PINK1
1219 phosphorylates ubiquitin to activate Parkin E3 ubiquitin ligase activity. *J Cell Biol* 205: 143-
1220 153
1221 Katayama H, Kogure T, Mizushima N, Yoshimori T, Miyawaki A (2011) A sensitive and
1222 quantitative technique for detecting autophagic events based on lysosomal delivery. *Chem*
1223 *Biol* 18: 1042-1052
1224 Kazlauskaite A, Martinez-Torres RJ, Wilkie S, Kumar A, Peltier J, Gonzalez A, Johnson C,
1225 Zhang J, Hope AG, Peggie M *et al* (2015) Binding to serine 65-phosphorylated ubiquitin
1226 primes Parkin for optimal PINK1-dependent phosphorylation and activation. *EMBO Rep* 16:
1227 939-954
1228 Kirk R, Laman H, Knowles PP, Murray-Rust J, Lomonosov M, Meziane el K, McDonald NQ
1229 (2008) Structure of a conserved dimerization domain within the F-box protein Fbxo7 and the
1230 PI31 proteasome inhibitor. *J Biol Chem* 283: 22325-22335
1231 Koyano F, Okatsu K, Kosako H, Tamura Y, Go E, Kimura M, Kimura Y, Tsuchiya H, Yoshihara
1232 H, Hirokawa T *et al* (2014) Ubiquitin is phosphorylated by PINK1 to activate parkin. *Nature*
1233 510: 162-166
1234 Kraus F, Miron E, Demmerle J, Chitiashvili T, Budco A, Alle Q, Matsuda A, Leonhardt H,
1235 Schermelleh L, Markaki Y (2017) Quantitative 3D structured illumination microscopy of
1236 nuclear structures. *Nat Protoc* 12: 1011-1028
1237 Labun K, Montague TG, Krause M, Torres Cleuren YN, Tjeldnes H, Valen E (2019) CHOPCHOP
1238 v3: expanding the CRISPR web toolbox beyond genome editing. *Nucleic Acids Res* 47: W171-
1239 W174
1240 Lambert SA, Jolma A, Campitelli LF, Das PK, Yin Y, Albu M, Chen X, Taipale J, Hughes TR,
1241 Weirauch MT (2018) The Human Transcription Factors. *Cell* 172: 650-665

1242 Lazarou M, Jin SM, Kane LA, Youle RJ (2012) Role of PINK1 binding to the TOM complex and
1243 alternate intracellular membranes in recruitment and activation of the E3 ligase Parkin. *Dev*
1244 *Cell* 22: 320-333
1245 Lazarou M, Sliter DA, Kane LA, Sarraf SA, Wang C, Burman JL, Sideris DP, Fogel AI, Youle RJ
1246 (2015) The ubiquitin kinase PINK1 recruits autophagy receptors to induce mitophagy.
1247 *Nature* 524: 309-314
1248 Li J, Cai Z, Bomgarden RD, Pike I, Kuhn K, Rogers JC, Roberts TM, Gygi SP, Paulo JA (2021)
1249 TMTpro-18plex: The Expanded and Complete Set of TMTpro Reagents for Sample
1250 Multiplexing. *J Proteome Res* 20: 2964-2972
1251 Liu K, Jones S, Minis A, Rodriguez J, Molina H, Steller H (2019) PI31 Is an Adaptor Protein for
1252 Proteasome Transport in Axons and Required for Synaptic Development. *Dev Cell* 50: 509-
1253 524 e510
1254 McAlister GC, Nusinow DP, Jedrychowski MP, Wuhr M, Huttlin EL, Erickson BK, Rad R, Haas
1255 W, Gygi SP (2014) MultiNotch MS3 enables accurate, sensitive, and multiplexed detection of
1256 differential expression across cancer cell line proteomes. *Anal Chem* 86: 7150-7158
1257 McWilliams TG, Muqit MM (2017) PINK1 and Parkin: emerging themes in mitochondrial
1258 homeostasis. *Curr Opin Cell Biol* 45: 83-91
1259 Narendra D, Tanaka A, Suen DF, Youle RJ (2008) Parkin is recruited selectively to impaired
1260 mitochondria and promotes their autophagy. *J Cell Biol* 183: 795-803
1261 Narendra DP, Jin SM, Tanaka A, Suen DF, Gautier CA, Shen J, Cookson MR, Youle RJ (2010)
1262 PINK1 is selectively stabilized on impaired mitochondria to activate Parkin. *PLoS Biol* 8:
1263 e1000298
1264 Ng MYW, Wai T, Simonsen A (2021) Quality control of the mitochondrion. *Dev Cell*
1265 Okatsu K, Koyano F, Kimura M, Kosako H, Saeki Y, Tanaka K, Matsuda N (2015)
1266 Phosphorylated ubiquitin chain is the genuine Parkin receptor. *J Cell Biol* 209: 111-128
1267 Ordureau A, Heo JM, Duda DM, Paulo JA, Olszewski JL, Yanishevski D, Rinehart J, Schulman
1268 BA, Harper JW (2015) Defining roles of PARKIN and ubiquitin phosphorylation by PINK1 in
1269 mitochondrial quality control using a ubiquitin replacement strategy. *Proc Natl Acad Sci U S*
1270 *A* 112: 6637-6642
1271 Ordureau A, Kraus F, Zhang J, An H, Park S, Ahfeldt T, Paulo JA, Harper JW (2021) Temporal
1272 proteomics during neurogenesis reveals large-scale proteome and organelle remodeling via
1273 selective autophagy. *Mol Cell*
1274 Ordureau A, Paulo JA, Zhang J, An H, Swatek KN, Cannon JR, Wan Q, Komander D, Harper JW
1275 (2020) Global Landscape and Dynamics of Parkin and USP30-Dependent Ubiquitylomes in
1276 iNeurons during Mitophagic Signaling. *Mol Cell* 77: 1124-1142 e1110
1277 Ordureau A, Paulo JA, Zhang W, Ahfeldt T, Zhang J, Cohn EF, Hou Z, Heo JM, Rubin LL, Sidhu
1278 SS *et al* (2018) Dynamics of PARKIN-Dependent Mitochondrial Ubiquitylation in Induced
1279 Neurons and Model Systems Revealed by Digital Snapshot Proteomics. *Mol Cell* 70: 211-227
1280 e218
1281 Ordureau A, Sarraf SA, Duda DM, Heo JM, Jedrychowski MP, Sviderskiy VO, Olszewski JL,
1282 Koerber JT, Xie T, Beausoleil SA *et al* (2014) Quantitative proteomics reveal a feedforward
1283 mechanism for mitochondrial PARKIN translocation and ubiquitin chain synthesis. *Mol Cell*
1284 56: 360-375
1285 Paisan-Ruiz C, Guevara R, Federoff M, Hanagasi H, Sina F, Elahi E, Schneider SA,
1286 Schwingenschuh P, Bajaj N, Emre M *et al* (2010) Early-onset L-dopa-responsive parkinsonism
1287 with pyramidal signs due to ATP13A2, PLA2G6, FBXO7 and spatacsin mutations. *Mov Disord*
1288 25: 1791-1800

1289 Paulo JA, O'Connell JD, Gygi SP (2016) A Triple Knockout (TKO) Proteomics Standard for
1290 Diagnosing Ion Interference in Isobaric Labeling Experiments. *J Am Soc Mass Spectrom* 27:
1291 1620-1625
1292 Perez-Riverol Y, Bai J, Bandla C, Garcia-Seisdedos D, Hewapathirana S, Kamatchinathan S,
1293 Kundu DJ, Prakash A, Frericks-Zipper A, Eisenacher M *et al* (2022) The PRIDE database
1294 resources in 2022: a hub for mass spectrometry-based proteomics evidences. *Nucleic Acids*
1295 *Res* 50: D543-D552
1296 Pickrell AM, Youle RJ (2015) The roles of PINK1, parkin, and mitochondrial fidelity in
1297 Parkinson's disease. *Neuron* 85: 257-273
1298 Plubell DL, Wilmarth PA, Zhao Y, Fenton AM, Minnier J, Reddy AP, Klimek J, Yang X, David LL,
1299 Pamir N (2017) Extended Multiplexing of Tandem Mass Tags (TMT) Labeling Reveals Age and
1300 High Fat Diet Specific Proteome Changes in Mouse Epididymal Adipose Tissue. *Mol Cell*
1301 *Proteomics* 16: 873-890
1302 Rad R, Li J, Mintseris J, O'Connell J, Gygi SP, Schweppe DK (2021) Improved Monoisotopic
1303 Mass Estimation for Deeper Proteome Coverage. *J Proteome Res* 20: 591-598
1304 Rath S, Sharma R, Gupta R, Ast T, Chan C, Durham TJ, Goodman RP, Grabarek Z, Haas ME,
1305 Hung WHW *et al* (2021) MitoCarta3.0: an updated mitochondrial proteome now with sub-
1306 organelle localization and pathway annotations. *Nucleic Acids Res* 49: D1541-D1547
1307 Ravenhill BJ, Boyle KB, von Muhlinen N, Ellison CJ, Masson GR, Otten EG, Foeglein A,
1308 Williams R, Randow F (2019) The Cargo Receptor NDP52 Initiates Selective Autophagy by
1309 Recruiting the ULK Complex to Cytosol-Invading Bacteria. *Mol Cell* 74: 320-329 e326
1310 Sarraf SA, Raman M, Guarani-Pereira V, Sowa ME, Huttlin EL, Gygi SP, Harper JW (2013)
1311 Landscape of the PARKIN-dependent ubiquitylome in response to mitochondrial
1312 depolarization. *Nature* 496: 372-376
1313 Sauve V, Sung G, Soya N, Kozlov G, Blaimschein N, Miotto LS, Trempe JF, Lukacs GL, Gehring
1314 K (2018) Mechanism of parkin activation by phosphorylation. *Nat Struct Mol Biol* 25: 623-
1315 630
1316 Savitski MM, Wilhelm M, Hahne H, Kuster B, Bantscheff M (2015) A Scalable Approach for
1317 Protein False Discovery Rate Estimation in Large Proteomic Data Sets. *Mol Cell Proteomics*
1318 14: 2394-2404
1319 Schindelin J, Arganda-Carreras I, Frise E, Kaynig V, Longair M, Pietzsch T, Preibisch S, Rueden
1320 C, Saalfeld S, Schmid B *et al* (2012) Fiji: an open-source platform for biological-image
1321 analysis. *Nat Methods* 9: 676-682
1322 Schweppe DK, Eng JK, Yu Q, Bailey D, Rad R, Navarrete-Perea J, Huttlin EL, Erickson BK, Paulo
1323 JA, Gygi SP (2020) Full-Featured, Real-Time Database Searching Platform Enables Fast and
1324 Accurate Multiplexed Quantitative Proteomics. *J Proteome Res* 19: 2026-2034
1325 Schweppe DK, Prasad S, Belford MW, Navarrete-Perea J, Bailey DJ, Huguet R, Jedrychowski
1326 MP, Rad R, McAlister G, Abbatiello SE *et al* (2019) Characterization and Optimization of
1327 Multiplexed Quantitative Analyses Using High-Field Asymmetric-Waveform Ion Mobility
1328 Mass Spectrometry. *Anal Chem* 91: 4010-4016
1329 Stirling DR, Swain-Bowden MJ, Lucas AM, Carpenter AE, Cimini BA, Goodman A (2021)
1330 CellProfiler 4: improvements in speed, utility and usability. *BMC Bioinformatics* 22: 433
1331 Stolz A, Ernst A, Dikic I (2014) Cargo recognition and trafficking in selective autophagy. *Nat*
1332 *Cell Biol* 16: 495-501
1333 Tai YC (2022) timecourse: Statistical Analysis for Developmental Microarray Time Course
1334 Data. R package version 1.68.0. *http://wwwbioconductororg*

1335 Tyanova S, Cox J (2018) Perseus: A Bioinformatics Platform for Integrative Analysis of
1336 Proteomics Data in Cancer Research. *Methods Mol Biol* 1711: 133-148
1337 Vargas JNS, Wang C, Bunker E, Hao L, Maric D, Schiavo G, Randow F, Youle RJ (2019)
1338 Spatiotemporal Control of ULK1 Activation by NDP52 and TBK1 during Selective Autophagy.
1339 *Mol Cell* 74: 347-362 e346
1340 Vingill S, Brockelt D, Lancelin C, Tatenhorst L, Dontcheva G, Preisinger C, Schwedhelm-
1341 Domeyer N, Joseph S, Mitkovski M, Goebbels S *et al* (2016) Loss of FBXO7 (PARK15) results
1342 in reduced proteasome activity and models a parkinsonism-like phenotype in mice. *EMBO J*
1343 35: 2008-2025
1344 Wang Y, Yang F, Gritsenko MA, Wang Y, Clauss T, Liu T, Shen Y, Monroe ME, Lopez-Ferrer D,
1345 Reno T *et al* (2011) Reversed-phase chromatography with multiple fraction concatenation
1346 strategy for proteome profiling of human MCF10A cells. *Proteomics* 11: 2019-2026
1347 Wauer T, Simicek M, Schubert A, Komander D (2015) Mechanism of phospho-ubiquitin-
1348 induced PARKIN activation. *Nature* 524: 370-374
1349 Wong YC, Holzbaur EL (2014) Optineurin is an autophagy receptor for damaged
1350 mitochondria in parkin-mediated mitophagy that is disrupted by an ALS-linked mutation.
1351 *Proc Natl Acad Sci U S A* 111: E4439-4448
1352 Yamano K, Youle RJ (2013) PINK1 is degraded through the N-end rule pathway. *Autophagy*
1353 9: 1758-1769
1354 Zhang Y, Pak C, Han Y, Ahlenius H, Zhang Z, Chanda S, Marro S, Patzke C, Acuna C, Covy J *et*
1355 *al* (2013) Rapid single-step induction of functional neurons from human pluripotent stem
1356 cells. *Neuron* 78: 785-798
1357 Zuris JA, Thompson DB, Shu Y, Guilinger JP, Bessen JL, Hu JH, Maeder ML, Joung JK, Chen ZY,
1358 Liu DR (2015) Cationic lipid-mediated delivery of proteins enables efficient protein-based
1359 genome editing in vitro and in vivo. *Nat Biotechnol* 33: 73-80
1360